ISBN: 978-94-017-8538-9 (Print) 978-94-017-8539-6 (Online)

Chapter 6 in "Kim, K.-H., Chahine, G.L., Franc, J.-P., and Karimi, A. (ed.) "*Advanced Experimental and Numerical Techniques for Cavitation Erosion Prediction, Series Fluid Mechanics and Its Applications*" Vol. 106, Springer, Berlin, Germany, 2014."

MODELING OF CAVITATION DYNAMICS AND INTERACTION WITH MATERIAL

By

Georges L. Chahine

DYNAFLOW, INC.

www.dynaflow-inc.com

glchahine@dynaflow-inc.com

6.1 Introduction

Previous chapters focused for the most part on presenting and interpreting empirical data obtained from experimental investigations of various aspects of cavitation erosion. The efforts involved characterization of both the cavitation field and the resulting material permanent deformation and erosion. Interpretation of the results often relied on physical reasoning based on prior knowledge of the cavitating flow configurations studied, the basic dynamics of bubbles, and the response of materials to applied loads. The characterization of cavitation impulsive pressures relied on the response to the impulsive loads of pressure transducers or on the measurement of the permanent deformation of the material itself.

This chapter presents numerical modeling and simulation of the non-spherical dynamics of bubbles near rigid and deformable boundaries with known material elastic-plastic properties and examines the response of the material to the loads generated by bubble collapse. The study aims at isolating the influence of each of the various physical parameters (i.e., bubble size, distance from the wall, collapse driving pressure, and material properties) on the spatial and temporal distribution of impulsive pressures resulting from the bubble dynamics, and also on the material elasto-plastic deformations in response to these loads. Knowledge of the inter-relationships between these parameters allows for the transposition of the results from one condition to another.

The relevant numerical techniques are first described succinctly to provide the assumptions used and their limits of validity for the study of cavitation erosion mechanics, followed by the dynamics of a bubble near a rigid boundary. Scaling rules of the various characteristics of the bubble re-entrant jet parameters and the pressure pulse resulting from the collapse are then analyzed. The unsteady effects of generated impulse loads on the material deformation are subsequently discussed. The time history of material deformation is analyzed and implications for the inverse determination of the loads from permanent deformation in pitting tests are discussed.

6.2 Numerical models

Cavitating flow field, bubble dynamics, and dynamic material response are simulated numerically in this chapter using several numerical techniques briefly described below. These include:

- a boundary element method potential flow model for 3D bubble dynamics, 3DYNAFS-BEM© [1-7],
- a finite difference method compressible Euler flow solver, GEMINI [8-10], for bubble dynamics,
- a procedure to link incompressible-compressible flow approaches [11, 12], and
- a finite element structural dynamic code, DYNA3D [13], to model material and structural response.

6.2.1 Flow field models

a. Boundary element model

3DYNAFS-BEM© is a potential flow solver based on a boundary element method (BEM). The code solves the Laplace equation, $\nabla^2\phi = 0$, for the velocity potential, ϕ, with the velocity vector $\mathbf{u} = \nabla\phi$. A boundary integral method is used to solve the Laplace equation based on Green's theorem:

$$\int_\Omega \left(\phi\,\nabla^2 G - G\,\nabla^2\phi\right) d\Omega = \int_S \mathbf{n}\cdot\left[\phi\,\nabla G - G\,\nabla\phi\right] dS \qquad (6.1)$$

In this expression Ω is the liquid domain of integration having elementary volume $d\Omega$. The boundary surface of Ω is S, which includes the surfaces of the bubble and the nearby boundaries with an elementary surface dS. $\mathbf{n}$ is the local surface normal unit vector. $G = -1/|\mathbf{x}-\mathbf{y}|$ is Green's function, where $\mathbf{x}$ is a fixed point in Ω and $\mathbf{y}$ is a point on the boundary surface S. Eq. (6.1) reduces to Green's formula with $a\pi$ being the solid angle under which $\mathbf{x}$ sees the domain Ω:

$$a\pi\phi(\mathbf{x}) = \int_S \left[\phi(\mathbf{y})\frac{\partial G}{\partial n}(\mathbf{x},\mathbf{y}) - G(\mathbf{x},\mathbf{y})\frac{\partial\phi}{\partial n}(\mathbf{y})\right] dS \qquad (6.2)$$

with $a = 4$ if $\mathbf{x}$ is a point in the fluid, and $a = 2$ if $\mathbf{x}$ is a point on a smooth surface.
Eq. (6.2) provides a relationship between ϕ and $\partial\phi/\partial n$ at the boundary surface S. Thus, if either of these two variables (e.g., ϕ) is known everywhere on the surface the other variable (e.g., $\partial\phi/\partial n$) can be obtained. To solve Eq. (6.2) numerically, the BEM, which discretizes the surface of all objects in the computational domain into panel elements, is applied.

On a bubble surface S_b, ϕ satisfies a kinematic boundary condition, which expresses equality between the normal velocities of the liquid and the free surface:

$$d\mathbf{x}/dt\cdot\mathbf{n} = \nabla\phi\cdot\mathbf{n} \qquad \mathbf{x}\in S_b \qquad (6.3)$$

and a dynamic boundary condition:

$$\frac{\partial\phi}{\partial t} = -\frac{1}{2}|\nabla\phi|^2 + \frac{P_{amb} - P_b}{\rho} - g\,z\big|_{x\in S_b} \qquad (6.4)$$

where P_{amb} is the ambient pressure, $P_b(\mathbf{x},t)$ is the local pressure in the liquid at the bubble interface, and z is the vertical coordinate at point $\mathbf{x}$.

The pressure inside the bubble is assumed to be spatially homogeneous, and the bubble content is assumed to be composed of non-condensable gas, which follows a polytropic expansion/compression law with constant k. This leads to the following form of the normal stress boundary condition at the bubble interface:

$$P_b(\mathbf{x},t) = P_{go}\left[\frac{\mathcal{V}_o}{\mathcal{V}(t)}\right]^k + P_v - \gamma C \qquad (6.5)$$

where P_{go} is the initial pressure of the non-condensable gas and P_v is the water vapor pressure. $\mathcal{V}_o$ is the initial volume of the bubble, γ is the surface tension coefficient, and $C(\mathbf{x},t)$ is twice the local mean curvature at $\mathbf{x}$ given by:

$$C = \nabla \cdot \mathbf{n} \qquad \mathbf{n} = \pm \frac{\nabla f}{|\nabla f|} \tag{6.6}$$

where f is the equation of the surface. The appropriate sign is chosen so that the normal always points towards the liquid.

3DYNAFS-BEM© was developed specifically to solve three-dimensional potential flow problems including highly non-linear free surface dynamics, such as encountered in bubble dynamics, ocean dynamics, and time dependent interfaces separating two or more fluid phases. It handles the dynamics of cavitation bubbles or explosion bubbles near solid boundaries, deformable cells, or free surfaces [1-7, 11, 12, 14, 15]. 3DYNAFS-BEM© can be coupled with a structural code such as DYNA3D (see Section 6.2.2) for simulation of fluid-structure interaction problems [10, 13].

b. Compressible flow model

GEMINI is a compressible Euler equation solver developed by the Naval Surface Warfare Center, Indian Head division, based on a finite difference scheme. The code solves continuity and momentum equations for a compressible inviscid liquid in Cartesian coordinates, which can be written in the following format:

$$\frac{\partial Q}{\partial t} + \frac{\partial E}{\partial x} + \frac{\partial F}{\partial y} + \frac{\partial G}{\partial z} = S \tag{6.7}$$

$$Q = \begin{bmatrix} \rho \\ \rho u \\ \rho v \\ \rho w \\ \rho e_t \end{bmatrix} \quad E = \begin{bmatrix} \rho u \\ \rho u^2 + p \\ \rho uv \\ \rho uw \\ (\rho e_t + p)u \end{bmatrix} \quad F = \begin{bmatrix} \rho v \\ \rho vu \\ \rho v^2 + p \\ \rho vw \\ (\rho e_t + p)v \end{bmatrix} \quad G = \begin{bmatrix} \rho w \\ \rho wu \\ \rho wv \\ \rho w^2 + p \\ (\rho e_t + p)w \end{bmatrix} \quad S = \begin{bmatrix} 0 \\ 0 \\ 0 \\ \rho g \\ \rho gw \end{bmatrix} \tag{6.8}$$

where ρ is the liquid density, p is the pressure, u, v, and w are the velocity components in the x, y, z directions respectively, g is the acceleration of gravity, and $e_t = e + 0.5(u^2+v^2+w^2)$ is the total energy with e being the internal energy. Eq. (6.8) is applied to solve gas, water, or a mixture of both, with an equation of state, which relates pressure, density, and energy for each phase.

The code applies a high order Godunov-type method [16] to accurately capture the location of discontinuities such as shock waves and contact surfaces. A mixed cell algorithm [8] is applied to enable the code to simulate multi-phase and multi-material flows. GEMINI can be coupled with a structural code to predict the response of nearby structures, and can be linked to 3DYNAFS-BEM©, as described in Section 6.2.1.c, to model various stages of bubble collapse accurately and efficiently [3-7, 11, 12]. GEMINI has been validated against large scale experiments [8-10, 17, 18].

c. Incompressible / compressible link procedure

Modeling cavitation bubble collapse near boundaries has been extensively done using potential flow boundary methods for axisymmetric cases [19-23] and 3D cases [1-7, 24, 25]. The boundary element method can accurately describe re-entrant jet formation and provide its characteristics as functions of time since the bubble wall velocities (including the re-entrant jet velocity) are most often small relative to the sound speed in water until the final stage of the bubble collapse. On the other hand, during the bubble explosive growth, rebound, and at jet impact, compressible effects can be non-negligible. These phenomena may lead to shock wave formation and propagation, thereby requiring a compressible approach.

Each of the incompressible and compressible methods has its advantages and disadvantages in addressing cavitation or underwater explosion bubble dynamics. The BEM is efficient since it reduces the dimension of the problem by one: an axisymmetric problem (2D) is reduced to a 1D problem involving line integrals and a 3D problem is reduced to integrals over the surfaces enclosing the 3D domain. This allows very fine gridding for increased accuracy with reasonable computation time. 3DYNAFS-BEM© has been shown to provide re-entrant jet parameters and speed accurately [24, 25]. However, it has difficulty pursuing the computations beyond surface impacts (liquid-liquid when the re-entrant jet hits the opposite side of the bubble and liquid-solid when the re-entrant jet hits the nearby solid wall). On the other hand, compressible finite element models (e.g. [8]) are most adequate to model shock wave emission and propagation, liquid-liquid and liquid-solid impacts. These methods require, however, very fine grids and very small time steps to resolve shock wave fronts. This makes the compressible methods appropriate to model efficiently only the shock wave propagation stage of the bubble dynamics. Concerning the bubble-liquid interface and the re-entrant jet dynamics, the procedure in the finite element models is diffusive since the interface is not directly modeled, and re-entrant jet characteristics are less accurate than obtained with the BEM approach.

In order to take advantage of the strengths of both the BEM and compressible Euler methods, a hybrid method was developed to address underwater explosion bubble problems and is used here for cavitation erosion bubble dynamics problems. Underwater explosion bubble studies can provide good visualization and measurement since the maximum bubble sizes are in the range of meters rather than millimeters, and time scales are in seconds rather than microseconds. The large spatial and temporal scales enable one to measure the jet speed and the pressures generated at the boundary with high accuracy both in space and time [26-28].

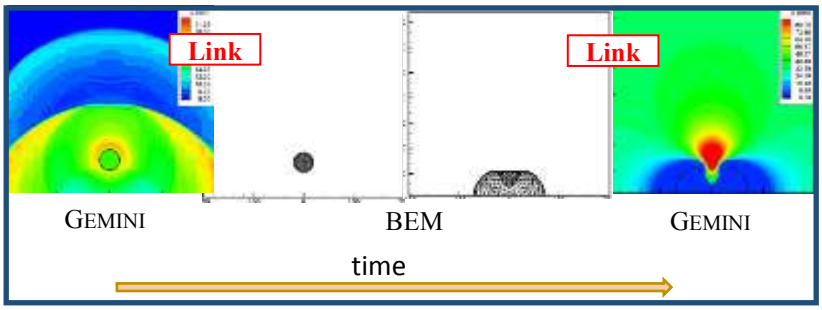

Fig. 6.1. Schematic showing the compressible-incompressible hybrid modeling procedure: link from GEMINI to 3DYNAFS-BEM© during bubble growth and shock propagation and from 3DYNAFS-BEM© to GEMINI following jet impact and shock emission.

In the hybrid method, geometry, grids, and flow information are exchanged between the two methods (compressible and incompressible) when needed ("Link" in Fig. 6.1). This link enables one method to pursue the problem resolution starting from the solution given by the other method. The compressible Euler solver GEMINI [8-12] is used during shock formation or during the impact (liquid-liquid or liquid-solid) stage on the materials, while the incompressible potential flow solver, 3DYNAFS-BEM© [1-7], is used during most of the bubble dynamics where the liquid velocities are very small compared to the sound speed. The details of the procedure and validation of this hybrid method can be found in [12].

For a bubble starting with an explosive growth to a maximum bubble size and then collapsing dynamically, the full compressible-incompressible-compressible link procedure in Fig. 6.1 is required, which consists of the following steps as time evolves:

1. The simulation is run with GEMINI until the shock fronts leave the computational domain and the remnant flow field can be assumed to be incompressible.
2. At that instance, the flow field variables (geometry, bubble pressure, boundary velocities) are transferred to 3DYNAFS-BEM© and are used to impose the non-zero normal velocities, $\partial\phi/\partial n$.
3. The bubble growth and collapse are solved using fine grids with 3DYNAFS-BEM© to obtain a good description of the re-entrant jet until this jet moves very close to the opposite side of the bubble.
4. The solution is then transferred back to GEMINI with the required flow variables (velocities, pressures, and densities at all space grid points).
5. The computation is then pursued with GEMINI to obtain the pressures due to re-entrant jet impact and remnant bubble ring collapse.

6.2.2 Structural model

DYNA3D is a non-linear explicit solid and structural dynamics solver based on the finite element method initially developed by the Lawrence Livermore National Laboratory [13, 29]. Based on a lumped mass formulation it solves the structure momentum equation:

$$\mathbf{M}\ddot{\mathbf{U}} + \mathbf{C}\dot{\mathbf{U}} + \mathbf{K}\mathbf{U} = \mathbf{F} \qquad (6.9)$$

where **U** is the displacement vector, **C** is the damping matrix, **K** is the stiffness matrix, and **F** is the matrix of the applied loads on the structure.

DYNA3D is appropriate for problems where high strain rate dynamics or stress wave propagation effects are important. Many material models are available to represent a wide range of material behavior, including elasticity, plasticity, thermal effects, rate dependence, damage, and failure of elements.

6.3 Impulsive loads due to bubble collapse near rigid boundary

Since the pioneering works of Plesset and Chapman [19], Ellis [20] and Naude and Ellis [21], a large number of numerical and experimental studies have been conducted to investigate the non-spherical collapse of a single bubble near a rigid boundary [22-28]. These studies have established the basis of our understanding of bubble re-entrant jet formation, emission of shock waves, and potential damage on the nearby surface. Simple conceptual extensions of the results from the idealized single bubble case to a multitude of bubbles in a cavitation field have also been done by several researchers [30-39]. More advanced studies involving bubble/bubble interactions and bubble cloud behavior as discussed in [40] remain as the subject of ongoing research.

Despite numerous studies to date, discussions among researchers continue about whether cavitation damage on the material surface results from shock loading or from localized loads of the re-entrant jet impact or from both. Major difficulties stem from the lack of comprehensive and accurate computational methods that account for all the important physics of the liquid, the bubble, the material, and their interactions. In the following sections, detailed analyses of computational results using the above described numerical methods are presented for the dynamics of non-spherical collapse of a single bubble interacting with a nearby solid boundary. The effects of the major parameters governing the bubble collapse dynamics are also presented, including the collapse driving pressure, the standoff distance to the wall, and the bubble size.

6.3.1 Re-entrant jet dynamics using BEM

Bubble collapse close to a rigid boundary can be highly asymmetrical and results in the formation of a fast re-entrant jet towards the boundary. High pressure loading on the boundary will develop from the impact of the jet on the boundary after it crosses the bubble. The intensity of the impact depends mainly on the relative distance between the bubble and the rigid boundary and on the "strength" of the collapse. Fig. 6.2 illustrates the bubble dynamics near a rigid boundary using an axisymmetric version of 3DYNAFS-BEM©.

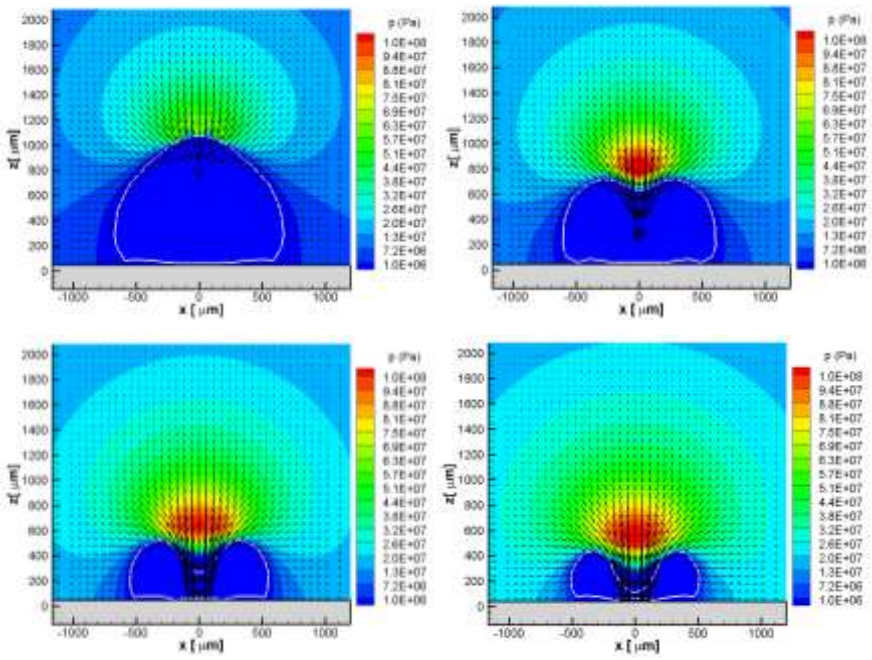

Fig. 6.2. Pressure and velocity field evolution during non-spherical bubble collapse near a wall predicted by 3DYNAFS-BEM© for a bubble with an initial radius of 10 μm and a gas pressure of 1 atm subjected to a pressure drop to -1 atm for 1 ms and then a steep pressure rise to 50 atm (t = 0). The bubble center is initially at a standoff 0.65 mm away from the wall. The maximum bubble radius is R_{max} = 1.3 mm at t = 0. The upper left contour is at bubble maximum volume (t = 20.6 μs). The other three contours are at t = 21.1 μs (upper right), t = 21.6 μs (lower left), and t = 21.8 μs (lower right).

Due to the asymmetry of the flow around the bubble created by the presence of the wall, a dipole-like pressure field develops in the bubble region farthest from the rigid wall. A high pressure region in the bulk of the liquid (red region) pushes down the bubble wall where the pressure is low (dark blue region) driving a high velocity flow along the axis of symmetry. This results in a high speed re-entrant jet that pierces the bubble from one side to the other, and then impacts the rigid wall when the bubble standoff to the wall is small. When the re-entrant jet impacts the wall, a water hammer-like pressure is generated and stresses the material. Later on, as the remaining bubble volume continues to shrink, high pressures are generated inside the ring bubble and a pressure wave or shock wave is emitted from the collapsing ring. The relative importance of the water hammer impact and the ring collapse depends on various physical parameters including the standoff distance between the initial bubble center location and the wall, and the bubble collapse driving pressure, $(P_{amb} - P_{bub})_0$.

6.3.2 Pressure loading from hybrid incompressible/compressible model

The hybrid compressible/incompressible approach is used to study the bubble growth and collapse near a rigid boundary in order to investigate the resulting impulsive pressure load. Figs. 6.3 through 6.8 illustrate the dynamics and present the pressures generated during the bubble collapse. A bubble with an initial radius of R_0 = 10 μm located at 75 μm above a rigid boundary is considered. The initial bubble internal pressure is 2.6 x 10^7 Pa (this could result from a bubble exiting a nozzle with an upstream pressure of 3,800 psi (26.2 MPa)) and the liquid ambient pressure is 10^5 Pa. In the absence of nearby boundaries the spherical bubble would expand to a maximum radius of R_{max} = 100 μm, a value easily computed using spherical bubble dynamics equations [41-43]. Fig. 6.3 shows the bubble contours at different times during the bubble growth and collapse. During the growth the bubble surface close to the rigid boundary flattens on the wall (actually, a thin water layer remains between the bubble and the wall as observed experimentally [7, 28]) while the surface farther from the wall expands freely until the pressure inside the bubble drops below the liquid dynamic pressure. As illustrated in Fig. 6.2 a localized high pressure region forces the water into the contracting bubble, generating a re-entrant jet which crosses the bubble and impacts the nearby wall. The right hand side of Fig. 6.3 clearly shows the evolution in time of the bubble shape and the re-entrant jet, which advances to strike the wall, while the thin layer between the bubble and the wall becomes thinner.

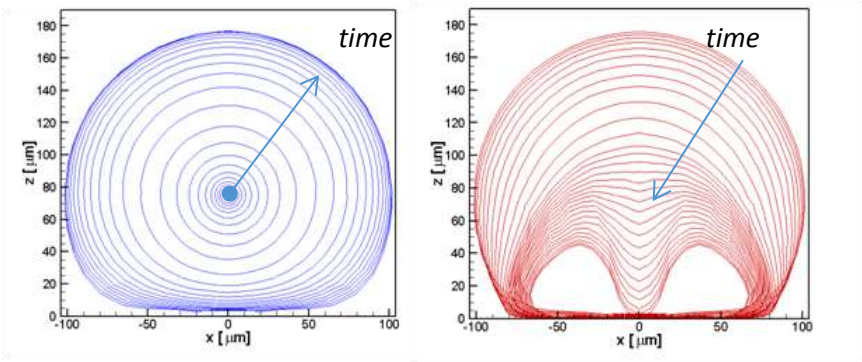

Fig. 6.3. Crosscuts showing bubble contour shapes during bubble growth (left) and collapse (right). Results obtained from 3DYNAFS-BEM© simulation. Note that a water layer remains between the bubble and the wall as observed experimentally with large scale bubbles. The bubble has an initial radius of R_0 = 10 μm and an initial gas pressure of 2.6 × 10^7 Pa and is initially at a standoff distance of 75 μm from a rigid wall, while the ambient pressure is 1 atm.

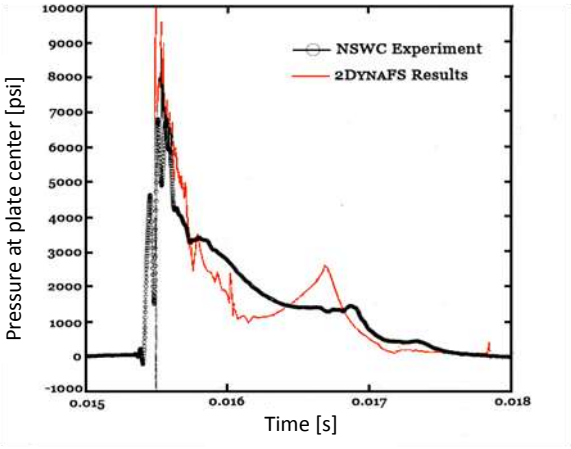

Fig. 6.4. Comparison between experimental measurements and numerical computations of the pressures due to bubble collapse on a rigid wall [7]. The bubble was generated by 10 g of TNT at a depth of 50 m on an instrumented circular plate. The generated bubble had a maximum radius of 0.18 m and the standoff from the plate was 0.14 m. The re-entrant jet speed was as high as 240 m/s. The axisymmetric version of 3DYNAFS-BEM© was used to conduct the numerical simulations and reproduced well the re-entrant jet impact pressure peak at t ~ 15.6 ms and to a lesser extent the bubble ring collapse pressure at about 16.7 ms. (1000 psi = 6.9 MPa).

In previous studies [7, 23, 45, 46] BEM computations continued beyond the jet touchdown by adding a sheet of vorticity at the impact interface between the advancing re-entrant jet and the bulk liquid, or a vortex ring at the edge of this surface. This allowed the computations to proceed beyond the point where the geometry becomes multi-connected and a vortex ring bubble is generated and collapses at the wall. This procedure was able to accurately predict the re-entrant jet impact pressure peak as illustrated in Fig. 6.4. However, the procedure is cumbersome, too sensitive to gridding, and often unstable. The new Link procedure described in the previous section is more robust and easy to use and has also produced validated output [11, 12].

The Link procedure continues the simulations starting from the 3DYNAFS-BEM© solution until a few computation steps before the jet impacts the opposite side of the bubble. The left side of Fig. 6.5 shows the 3DYNAFS-BEM© gridded bubble shape used to proceed with the compressible flow solution. The right side of Fig. 6.5 shows pressure contours from the first time step of GEMINI right after the solution was passed from 3DYNAFS-BEM©.

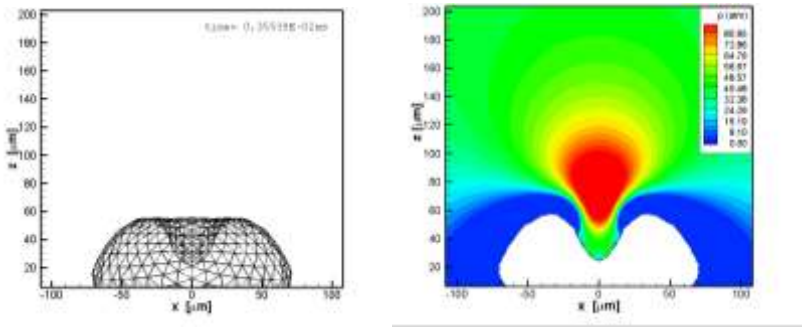

Fig. 6.5. 3DYNAFS-BEM© solution (left) where the solution was handed back to GEMINI and the first time step from GEMINI (right). The bubble has an initial radius of R_0 = 10 μm and an initial gas pressure of 2.6×10^7 Pa charged at a standoff distance of 75 μm from the rigid wall with an ambient pressure of 1 atm.

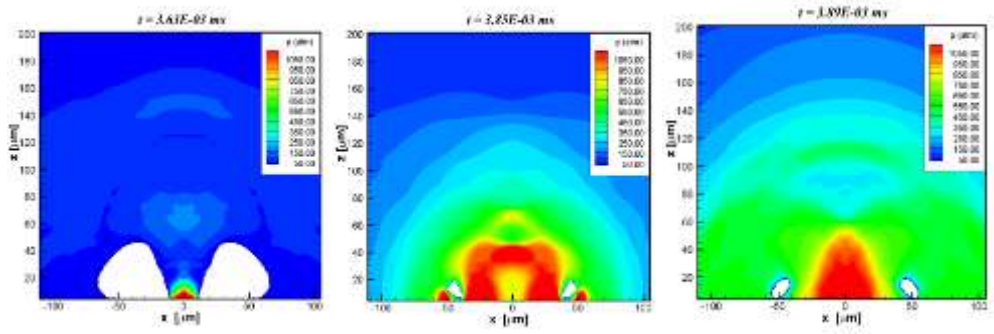

Fig. 6.6. Pressure contours at different instances of time due to jet impact and ring collapse obtained from GEMINI proceeding from the 3DYNAFS-BEM© solution. The bubble had an initial radius of R_0 = 10 μm and an initial gas pressure of 2.6 × 10^7 Pa charged at a standoff distance of 75 μm from the rigid wall with an ambient pressure of 1 atm.

Fig. 6.6 shows the pressure contours and the bubble dynamics from GEMINI at three subsequent times. At t = 3.63 μs, the jet impacts the wall generating a localized high pressure impact region on the axis leaving around it a bubble ring (white contours). At t =3.85 μs, the bubble ring has completed its collapse (the white contours reach the minimum) resulting in a ring like high pressure region on the wall around r = 50 μm. The high pressure or shock waves travel towards the axis resulting in a high pressure region near the axis, as shown at 3.89 μs in the last contours where the bubble ring is rebounding (white contours increasing area again).

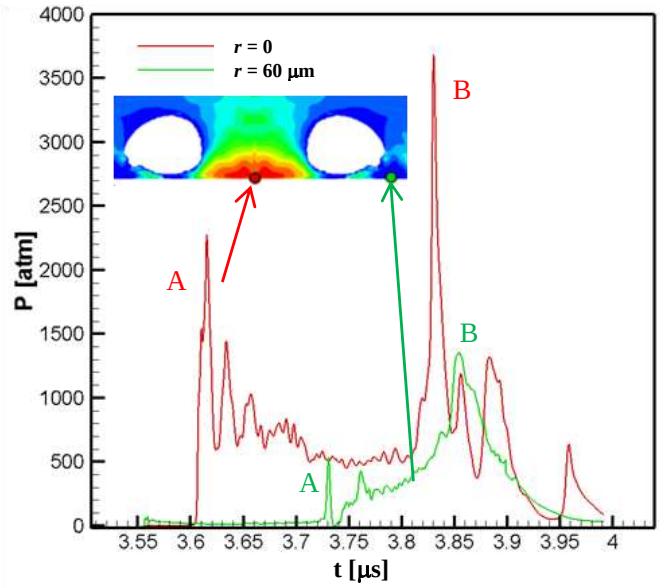

Fig. 6.7. Pressure due to bubble jetting and ring collapse monitored at two different radial locations at the wall, r = 0 and r = 60 μm. The bubble had an initial radius of R_0 = 10 μm and an initial gas pressure of 2.6 × 10^7 Pa at a standoff distance of 75 μm from the rigid wall while the ambient pressure was 1 atm. Pressure peaks A are due to the water hammer like pressure generated by the re-entrant jet impact, while pressure peaks B are due to ring bubble collapse.

Fig. 6.7 shows the time history of the pressure computed at two locations on the wall indicated in the insert: the bubble axis of symmetry and a point at a radial distance of 60 μm. There is a marked difference between the signals computed at the two locations.

The point on the axis sees distinctly two pressure peaks: the first peak at t = 3.615 μs (red A) is at the moment of the re-entrant jet impact. The second peak (red B) at 3.83 μs corresponds to the bubble ring collapse. A toroidal pressure wave emanates from the collapsing bubble ring and then focuses and amplifies at the axis of symmetry, r = 0. This results in a very sharp high peak (red B) shown in the figure.

The point at r = 60 μm does not sense the jet impact at t = 3.615 μs as it is outside the jet impact region (~10μm). However, it feels the effect of the jet impact a little later at t = 3.73 μs (green A). The second peak (green B) due to the ring collapse is clearly detected because r = 60 μm is close to the ring collapse location.

It is to be noted that for such small cavitation bubbles, the distinction between the two events is extremely difficult experimentally using conventional transducers. For spark generated bubbles or underwater explosion bubbles however, these differences in the signal can be clearly measured [25-28]. The difference between the measured signals on-axis and off-axis, further illustrated in Fig. 6.8, could explain why discussions are still on-going about whether cavitation damage is from shock waves or from jets as time histories of the pressure appear different depending on the precise location of the gauge.

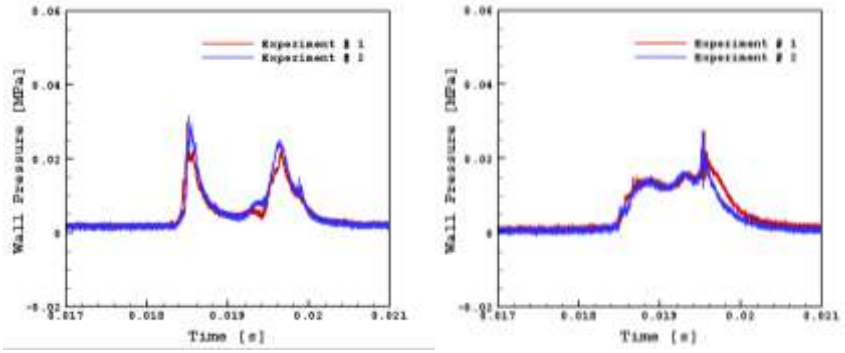

Fig. 6.8. Wall pressures recorded during the collapse and rebound of a spark generated bubble located at 1.8 cm from a vertical wall. The equivalent maximum bubble radius was 2.4 cm and the static pressure at the bubble center was 8,590 Pa for the left figure and 7,900 Pa for the right figure. In the left figure the PCB 101A04 piezoelectric transducer was located at the bubble re-entrant jet impact location. In the right figure the transducer was 0.5 cm off-center. These tests were conducted in the DYNAFLOW spark test facility.

6.3.3 Effect of local pressure driving bubble collapse

The speed of the bubble collapse depends on the pressure driving the dynamics, e.g. the difference of pressures between the outside and the inside of the bubble. This pressure difference can result from the bubble being driven into a stagnation region where the pressure is very high (e.g. in cavitating jets), or from very high pressure waves generated by the collapse of bubble clouds. The local pressure driving the individual bubble collapse will vary between scales (see [40]). In order to quantify the effect of the driving pressure on the loads, the hybrid incompressible (3DYNAFS-BEM©) / compressible (GEMINI) approach was used for different driving pressures. For illustration, we consider bubbles, which have grown to a maximum radius of 2 mm at which point the internal pressure is close to the liquid vapor

pressure, and are then subjected to a collapse driving pressure, $P_{collapse}$, varying from 10^5 Pa (1 atm) up to 1.5 x 10^7 Pa (150 atm). In all cases the bubble started collapsing when its center was at a distance of 1.5 mm from a rigid wall that is for a normalized standoff distance of 0.75.

For all values of the driving pressure, a strong re-entrant jet develops and advances to hit the rigid wall with a large impact velocity. As illustrated in Fig. 6.9, the jet velocity increases with the square root of the driving pressure, $P_{collapse}$. This is consistent with previous studies of bubble collapse dynamics [44]. In the present case, the re-entrant jet velocity can be approximated by:

$$V_{jet} \sim 4.6\sqrt{P_{collapse}/\rho} \qquad (6.10)$$

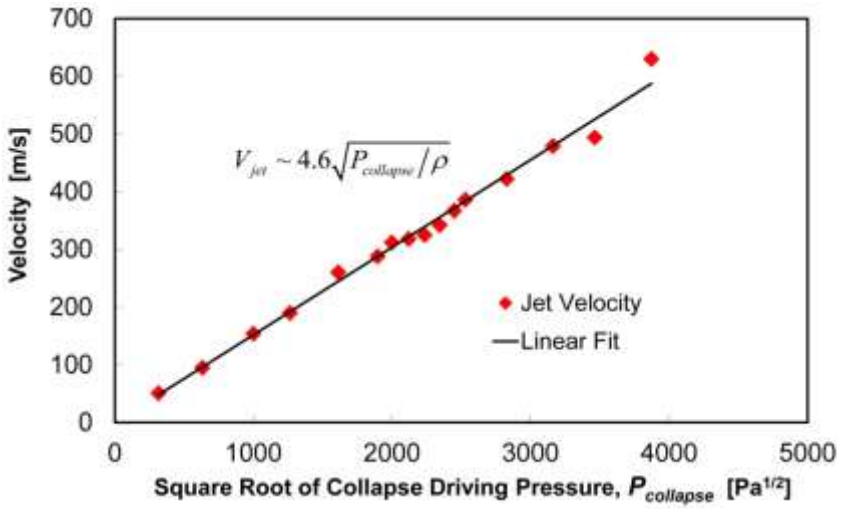

Fig. 6.9. Relationship between the re-entrant jet velocity and the pressure driving the bubble collapse. The red diamond symbols are jet impact velocities computed by the 3DYNAFS-BEM© for different ambient pressures, and the black curve is a linear fit. Maximum bubble radius 2 mm. Distance of bubble center to wall 1.5 mm (normalized standoff distance of 0.75).

Fig. 6.10 shows the peak pressure on the wall from bubble collapse for selected cases in Fig. 6.9. This figure confirms the classical view that the pressures due to bubble collapse are scaled by the water hammer impact pressure [23, 42] which is given by:

$$P_{water\ hammer} = \rho c V_{jet} \qquad (6.11)$$

where ρ is the density of the liquid, c is the speed of sound, and V_{jet} is the jet velocity at impact. The $P_{water\ hammer}$ is the pressure on a flat solid surface exerted by a water column with a flat surface [23, 41-43]. As the flatness of the re-entrant jet tip varies with the intensity of the collapse, so does the efficiency of the impact. As shown in Fig. 6.10, one can estimate the impulsive pressure generated by the jet impact using:

$$P_{impulse} \sim 0.6\rho c V_{jet} \qquad (6.12)$$

The figure shows that the impact efficiency improves for the higher collapse driving pressures and a factor larger than 0.6 applies at these higher pressures.

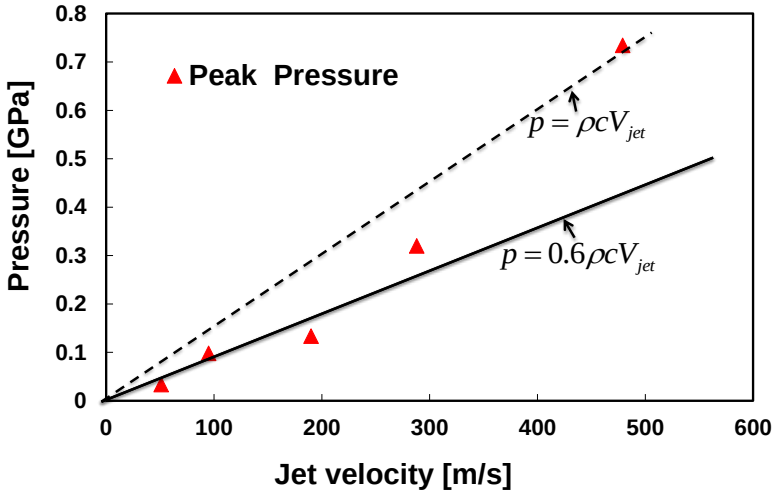

Fig. 6.10. Relationship between the peak impact pressure and the jet velocity. The jet velocities are computed by the 3DYNAFS-BEM© at the time of jet impact. The red symbols are from computed maximum peak impact pressures by the hybrid approach (3DYNAFS-BEM© and GEMINI) (such as in Fig. 6.11). Maximum bubble radius 2 mm, distance from bubble center to wall 1.5 mm (normalized standoff distance of 0.75).

The details of the impact pressure versus time at the center point on the wall are shown in Fig. 6.11 for a set of collapse driving pressures for the same bubble collapse conditions as in the previous two figures. All pressure histories have been shifted to the same starting point to show times from the moment of jet impact at the wall. As previously discussed in Fig. 6.7, all of the signals but the one corresponding to $P_{collapse} = 4$ atm clearly exhibit at least two pressure peaks following the impact: the first corresponds to re-entrant jet tip liquid impact at the wall, and the second (and sometimes third) is generated by the bubble ring collapse (and sometimes second collapse after rebound) and the focusing of the resulting shock wave on the jet/wall axis.

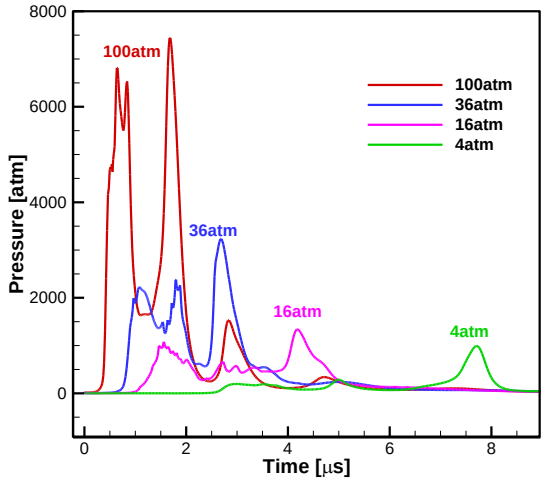

Fig. 6.11. Pressures computed by the hybrid approach (3DYNAFS-BEM© and GEMINI) at a nearby rigid wall from the collapse of a bubble under different bubble collapse driving pressures. Initial maximum bubble radius, R_{max} = 2 mm. Initial standoff distance, X = 1.5 mm.

The characteristic time of the bubble dynamics is the Rayleigh time expressed as:

$$T_{Rayleigh} = R_{\max}\sqrt{\rho / P_{collapse}} \qquad (6.13)$$

As the driving pressure increases, $T_{Rayleigh}$ decreases and the spacing between the two peaks also decreases. On the other hand, as the jet speed increases, the resulting jet impact pressure and the bubble ring collapse pressure increase.

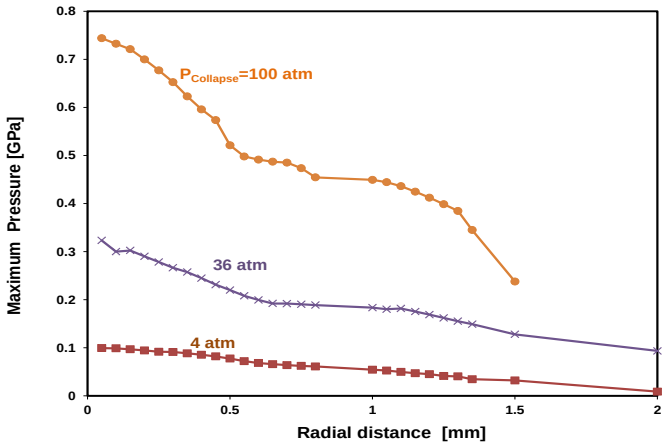

Fig. 6.12. Maximum pressures versus radial distance generated at a nearby rigid wall from the center of a bubble collapsing under different driving pressures. Initial maximum bubble radius, R_{max} = 2 mm. Initial standoff distance, X = 1.5 mm.

The above observations provide a scaling of the level of the impulsive pressure generated on the wall at bubble collapse, $P_{impulse}$, as a function of the ambient pressure driving the bubble collapse, $P_{collapse}$, combining Eqs. (6.10) and (6.12):

$$P_{impulse} \sim 2.76\, c\sqrt{\rho P_{collapse}} \qquad (6.14)$$

The pressure distribution function, $p(\mathbf{M},t)$, at the impact location **M** has a lateral extent, which scales with the bubble maximum radius. This is illustrated in Fig. 6.12, which shows that the maximum pressure drops off rapidly radially away from the jet axis. It decays to practically half its maximum value at a distance of R_{max} from the axis.

6.3.4 Effect of standoff

The illustrations presented in the previous sections corresponded to a normalized standoff between the bubble center and the wall, X/R_{max} = 0.75, which is in the range of maximum pressures generated on a nearby rigid wall [25]. The fastest velocity at the bubble wall increases as the bubbles move away from the rigid boundary. This applies also to the re-entrant jet velocity. However, for a larger standoff, e.g. $X/R_{max} > 1.25$, the re-entrant jet, after penetrating and piercing the opposite bubble side, has to advance in water before reaching the wall. This results in a significant loss of energy that attenuates the jet speed and subsequent impact pressure. On the contrary, for the small standoff distances, $X/R_{max} < 0.75$, the re-entrant jet hits the wall directly but does not have time to fully develop and attain a large speed because of the short distance. Indeed, as we will see later (e.g. Fig. 6.16), the jet speed is a relatively strong function of time.

Fig. 6.13 illustrates the effect of standoff by showing bubble contours during collapse for three standoffs: X = 1.05, 1.25, and 2.0 R_{max}. The bubble is initially spherical with a radius 100 μm, and is in equilibrium with the surrounding liquid when the ambient pressure is 1 atm. The bubble is then subjected to a sudden ambient pressure rise to 34 atm. For the farthest distance (X = 2.0 R_{max}), the bubble starts a quasi-spherical collapse, then a relatively wide re-entrant jet develops and strikes the opposite side of the bubble far from the wall. As the bubble initial standoff distance is reduced, the bubble elongates perpendicular to the wall during collapse and the re-entrant jet shape becomes more pointed. Moreover, the motion of the bubble surface closer to the rigid boundary is significantly reduced almost to zero for X/R_{max} = 1.05, while it is almost equal to R_{max} for X/R_{max} = 2.

Fig. 6.14 shows the pressures due to bubble collapse at the center of the nearby rigid boundary. The left and right figures present computations for a bubble with initial maximum radii of 10 μm and 500 μm, respectively. The bubbles are initially spherical and in equilibrium with the surrounding liquid at a pressure of 1 atm. Three standoff distances are considered as in Fig. 6.13: X/R_{max} = 1.05, 1.25 and 2.0. Unlike previous cases in Fig. 6.13 where the initial bubble radius was 100 μm, it is here 10 and 500 μm. The reason for the choice of two very different radii is to highlight the fact that the amplitude of the pressure generated by the bubble collapse for the same driving condition is practically independent of the initial bubble radius. This is very well highlighted in Fig. 6.14, where, for the three standoff distances, there is practically no difference in the amplitude of the pressures between the 10 μm (left) and the 500 μm (right) cases. The time scale on the other hand, follows the $T_{Rayleigh}$ scaling (Eq. (6.13)). The first peaks in Fig. 6.14 (~ 0.18 μs and ~ 9 μs on the left and right figure respectively) occur at re-entrant jet impact. The timing of the re-entrant jet impact is seen to scale with R_{max} and is 50 times larger for the 500 μm bubble (~ 9.5 μs) than for the 10 μm bubble (~ 0.19 μs). The same applies for the time delay between the jet impact and the bubble ring collapse (~ 0.2 μs vs. ~ 0.004 μs).

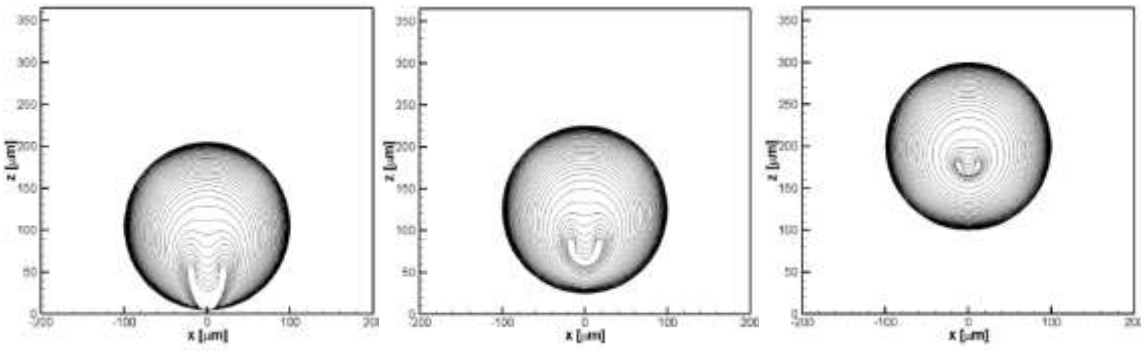

Fig. 6.13. Bubble shape variations during collapse of a 100 μm radius bubble under a collapse driving pressure of 34 atm at three standoffs X, initial distance from the bubble center to the wall: X/R_{max} = 1.05 (left), X/R_{max} = 1.25 (middle), and X/R_{max} = 2 (right). R_{max} =100 μm is the initial maximum bubble size. The bubble has an initial gas pressure of 1 atm.

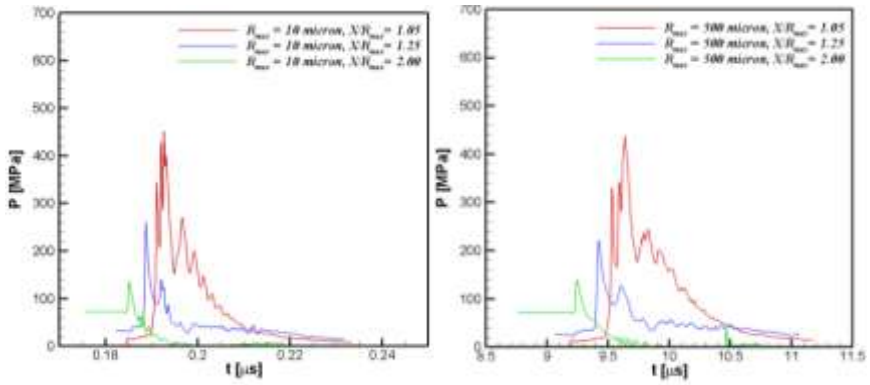

Fig. 6.14. Comparisons for R_{max} = 10 μm (left) and R_{max} = 500 μm (right) of the pressure on the wall at the bubble axis due to re-entrant jet impact and bubble ring collapse for different normalized standoffs: X/R_{max} = 1.05 (red), 1.25 (blue), and 2.0 (green). The bubbles have an initial gas pressure of 1 atm and are subjected to an ambient pressure of 34 atm. Notice the very close correspondence of the amplitudes between the two cases indicating very small sensitivity of the pressure amplitude to the bubble initial radius, and a ratio of 50 between the times indicating linear relationship between the bubble radius and the time scale.

Fig. 6.14 also shows clearly the effect of the standoff distance on the wall pressures. As the standoff decreases from X/R_{max} = 2.0 to 1.25 and 1.05, the bubble collapse period (i.e. the time from bubble maximum volume to minimum volume) increases, as well documented in the literature [42, 43, 47, 48]. This results in the re-entrant jet impacting the wall later for closer standoffs [47, 48]. This is illustrated in Fig. 6.14 by the first pressure peak occurring at a later time for the smaller standoff. On the other hand, as X/R_{max} increases, the impact pressures decrease, while the pressure peak due to the bubble ring collapse becomes too low to discern in the pressure trace. In the literature [22, 23, 45, 46], X/R_{max} = 1.5 is the typical case studied and this may explain why less emphasis has been placed in the past on the presence of the second pressure peak.

6.3.5 Influence of bubble size

This section examines the importance of bubble size on the impulsive pressure loads. To do so, bubble radii ranging from 10 to 500 μm are considered. Initial conditions as in the previous section are considered: all the bubbles are assumed to be spherical and in equilibrium with the liquid at an ambient pressure of 1 atm. One should note that this results in different initial internal bubble pressures due to the presence of surface tension. The bubbles are then subjected to a rise in the ambient pressure to 34.5 atm when they are near a rigid boundary located at X/R_{max} = 1.05, 1.25 or 2.0.

Fig. 6.15 presents the time variations of the bubble equivalent radius (i.e. radius of a sphere with the same volume) for the bubble sizes considered and for two normalized standoff conditions, X/R_{max} = 1.05 and 2. Radii and times are normalized respectively by the initial maximum radius, R_{max}, and by the Rayleigh time (Eq. (6.13)). The figure illustrates that for a given standoff, the normalized curves do not distinguish between the different initial bubble sizes. However, the standoff distance shows a distinct effect on the bubble collapse periods, i.e. larger periods for the smaller normalized distances, X/R_{max} and the presence of the wall slows down the collapse. In Fig. 6.15, the solution of the Rayleigh-Plesset equation in an infinite fluid is also presented as a reference.

Fig. 6.16 shows the re-entrant jet speed versus time for different bubble sizes and for the two normalized standoff distances, X/R_{max} = 1.05 and 2. It is interesting to note that for a given nondimensional standoff,

the dimensional jet velocity curves versus normalized times are insensitive to the bubble size especially for the smaller standoff distances, and are mostly controlled by the collapse driving pressure and the normalized distance from the wall. Near the wall, asymmetry is predominant and bubble size does not show an important effect. Farther from the wall, surface tension and initial gas pressure, which introduce nonlinear effects not captured by the Rayleigh scaling, have a non-negligible effect on the jet velocity and are responsible for the differences between the curves.

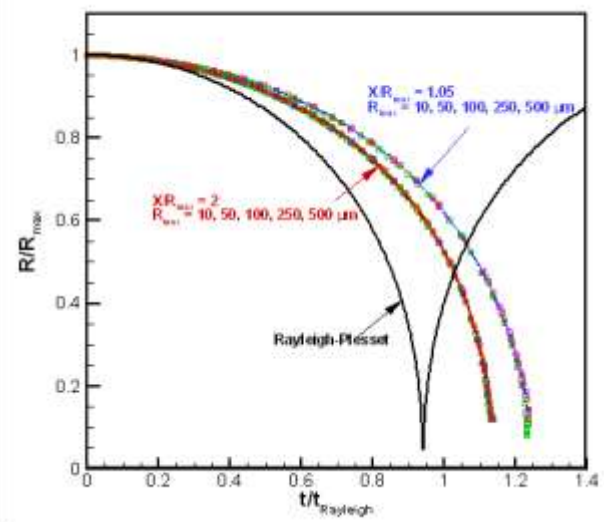

Fig. 6.15. Comparison of the time history of the normalized bubble equivalent radius for initial bubble maximum radii of 10, 50, 100, 250 and 500 μm at X/R_{max} = 1.05 (blue line) and X/R_{max} = 2.00 (red line). All the bubbles have an initial gas pressure of 1 atm and are subjected to an ambient pressure of 34.5 atm. The bubble equivalent radius is normalized by R_{max} while the time scale is normalized by the Rayleigh time.

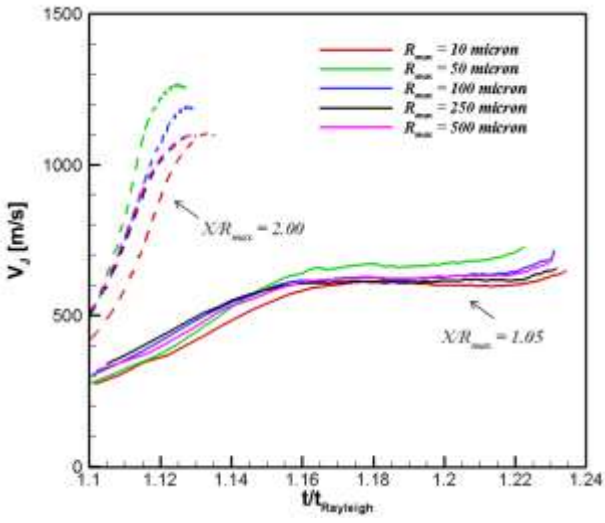

Fig. 6.16. Comparison of the time history of the re-entrant jet velocity for initial maximum bubble radii of 10, 50, 100, 250 and 500 μm at X/R_{max} = 1.05 (solid lines) and X/R_{max} = 2 (dashed lines). All the bubbles have an initial gas pressure of 1 atm and are subjected to a sudden pressure jump to 34 atm driving the bubble collapse.

Fig. 6.16 also shows that the normalized standoff distance has a very significant effect on the terminal velocities of the re-entrant jet. For instance, for X/R_{max} = 1.05 the terminal jet velocity is approximately 650 m/s while for X/R_{max} = 2.00 it is in the range of 1,100 to 1,300 m/s.

Fig. 6.17 compares the normalized time histories of the wall pressures for X/R_{max} = 1.05 and 1.25 for various bubble sizes. The collapse of all pressure loading curves for a given standoff is remarkable. This highlights that, independent of the bubble size, the pressures generated at the wall (see Eq. (6.14)) scale very well with the water hammer pressure due to the re-entrant jet velocity, which depends only on the driving pressure (see Eq. (6.10)). The time also scales very well with the Rayleigh time (see Eq. (6.13)). The normalized peak pressure for X/R_{max} = 1.05 is of the order of $0.5\rho cV_{jet}$, while for X/R_{max} = 1.25 it decreases to about $0.25\rho cV_{jet}$.

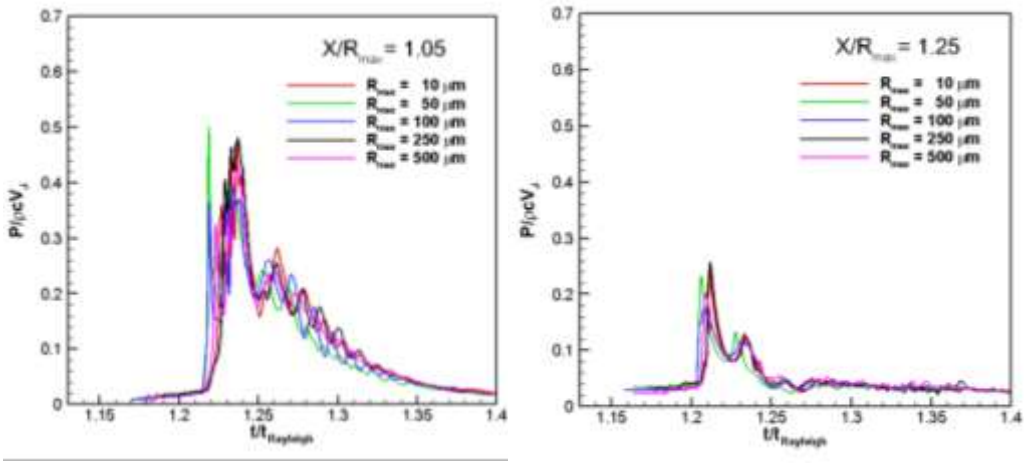

Fig. 6.17. Time history of the normalized pressure on the wall at the axis (r = 0) for different bubble sizes at two normalized standoff distances: X/R_{max} = 1.05 (left) and 1.25 (right). All the bubbles have an initial gas pressure of 1 atm and are subjected to a sudden pressure rise of 34.5 atm driving the bubble collapse.

The variations of the pressure on the wall with time and with the radial direction are illustrated in Fig. 6.18. This figure provides a picture of the dynamic evolution of the pressure loading in space and time for two bubble standoff distances. For X/R_{max} = 1.05, the radial pressure distribution at different instants shows that as the bubble collapses the pressure on the axis gradually increases until it reaches the first peak (from the re-entrant jet impact) followed by a second peak (from the bubble ring collapse) then it gradually decays and has oscillations from reflected waves through the thickness of the plate (details are discussed in Section 6.4). In the radial direction the impact wave propagates away from the axis with the two above described peaks moving outwards while rapidly decaying. The location of the peak pressure moves outward radially as a ring wave. Due to wave propagation at a finite time after the impact the radial distribution resembles the time trace of the pressure and contains the two peaks described earlier (re-entrant jet and ring collapse). For X/R_{max} = 2.00 the peaks are significantly lower, and owing to the larger standoff, only the pressure/shock front generated by the bubble collapse reaches the wall affecting a larger area and then gradually dissipates in time.

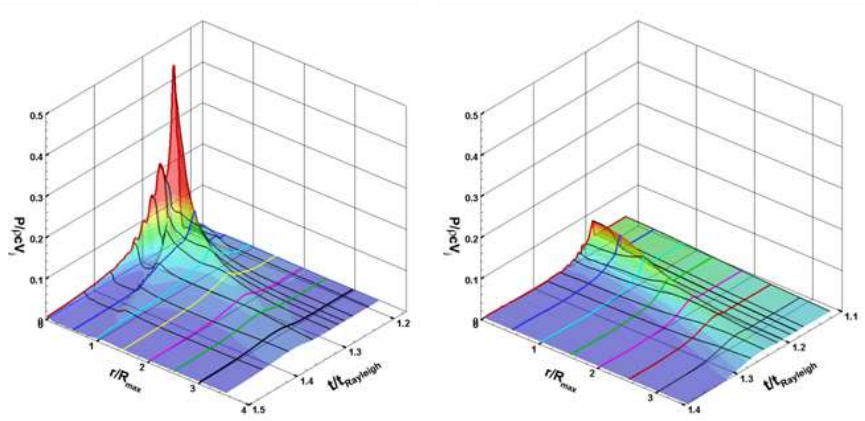

Fig. 6.18. Variations of the pressure at the wall with time and with the radial direction for two standoffs X/R_{max} = 1.05 (left) and 2.00 (right). The bubble has an initial radius R_{max} = 10 μm and is in balance with an ambient pressure of 1 atm. It is then subjected to a sudden pressure rise to 34 atm.

6.4 Material deformation from cavitation impulsive loads

In the previous section, mostly the dynamics of a collapsing bubble near a *rigid* boundary was discussed. The simulations enabled computation and analysis of the idealized impulsive loads that the collapse would produce at the nearby boundary in the absence of response from the boundary itself. A two-step procedure for the computation of the interactions would then use this load as input to evaluate the resulting material stresses, strains, and overall deformations. This is one-way coupled fluid-structure interaction (FSI) approach. A more accurate analysis would involve two concurrent computations (bubble dynamics with liquid flow and structural mechanics with solid response) enabling a two-way coupled mode. This two-way coupled approach is necessary when deformations and deformation speeds and accelerations are significant enough to affect the bubble dynamics. This is the case for very large impulsive loads and/or very flexible or deformable materials. In this section, a finite element model is presented first for a canonical problem of a single bubble collapsing in the vicinity of a flat circular plate with a finite thickness, followed by computational results using one-way and two-way coupled FSI approaches. The effects of the collapse driving pressure and the bubble size on the material permanent deformation (pitting) are shown.

To further understand the mechanics at play, synthetic cases of idealized loads are then considered to illustrate the effects of the amplitude, duration, and radial extent of the loads on the permanent deformation. The developed knowledge and results provide input for the development of an inverse procedure to deduce loads from pitting results.

The permanent deformation equations proposed from nano-indentation analysis (see Section 3.4) are then used to deduce the imparted impulsive loads and compared with the actual loads input in the computations.

6.4.1 Finite element modeling

To enable the fluid-structure interaction simulations the Link procedure described in Section 6.2.1.c is exercised while the fluid codes are coupled with the structure code briefly introduced in Section 6.2.2, DYNA3D [13]. For the present application, the large significant impulsive pressure loads occur only after the re-entrant jet fully penetrates the bubble and strikes the nearby wall, and therefore FSI computations using the compressible code, GEMINI, and DYNA3D are relevant. For the single bubbles considered in this section axisymmetric options of these codes are exercised.

A finite element mesh for a circular plate with 1 m radius and 5 mm thickness is generated using the axisymmetric setup illustrated in Fig. 6.19. The size of the plate (i.e. computational domain) was selected to be sufficiently large relative to the micron size bubbles, in order to minimize numerical reflections from the edges of the plate. The mesh elements near the axis of the plate are 5 μm by 5 μm. This fine element size was maintained up to 1.5 mm radius from the axis and down to 0.6 mm distance from the surface. From there on, the mesh size was gradually increased both in the outward and in the thickness direction. The mesh stretch factor was 10% up to a radius of 10 cm, and then increased to 30% beyond 10 cm. This resulted in 377 elements in the radial direction and 258 elements in the thickness direction.

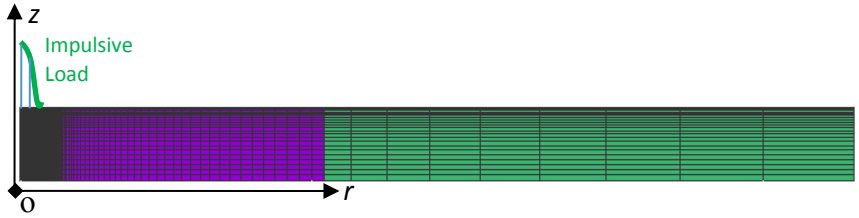

Fig. 6.19. Finite element axisymmetric grid used in DYNA3D to study elasto-plastic material response to loads due to collapsing cavitation bubbles. The cells in the dark region near $r = 0$ are 5 μm by 5 μm. The mesh size was stretched by a factor of 10% in the magenta region and 30% in the green region. (Note: r and z do not have the same scale.)

The boundary conditions used for the simulations were as follows:

- An imposed unsteady pressure load at the 'free' material-liquid interface provided by the fluid solution (or a given function in the synthetic runs).
- Rigid boundary condition at the bottom of the plate, i.e. no displacements in the plate thickness direction.
- No reflection boundary conditions at the edge of the plate.

An isotropic elasto-plastic material model was used for the computations. Material properties such as Young's modulus, yield stress, density, and failure strain were specified as input. The materials considered in this study included the materials experimentally studied in previous chapters, i.e. aluminum alloy Al 7075, stainless steel A2205, and NAB. In addition, a softer material, Al 1100-H19, was used in some of the computations. Bilinear representation of the stress-strain curves (see Fig. 6.20) of the four materials were used for DYNA3D. The first line of slope E, the Young's modulus, represented the elastic portion of the behavior. This intersected the linearly modeled plastic behavior beyond the yield point. The slope of the second portion is the tangent modulus. These properties were obtained from data published in the literature [49] and presented in Fig. 6.20 and Table 6.1.

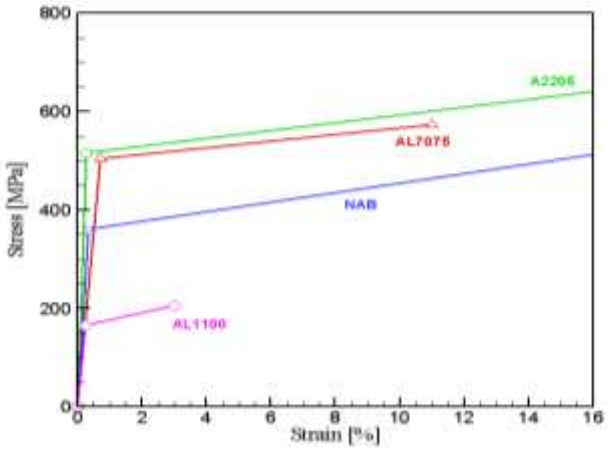

Fig. 6.20. Stress-strain curves utilized in DYNA3D to model elasto-plastic behavior of the materials studied. These were obtained from information available online [49].

Table 6.1. Material properties used for DYNA3D computations. These were obtained from available information online [49].

Material	Yield Stress [MPa]	Young's Modulus [GPa]	Tangent Modulus [MPa]	Elongation at Failure	Density [g/cm^3]
Al 7075	503	71.7	670	0.11	2.81
SS A2205	515	190	705	0.35	7.88
NAB	360	110	1216	0.25	7.64
Al 1100-H19	165	69	1449	0.03	2.71

6.4.2 Process of pit formation

In order to study the response of a solid material to impulsive loads from bubble collapse, pressures generated by the bubble collapse were applied to an elasto-plastic material. As long as the local stresses do not exceed the yield stress, the material deforms elastically during the loading and returns to its initial state once the load is relieved. However, once the yield point is exceeded anywhere in the material, permanent deformation occurs. An example is presented in Fig. 6.21 for the collapse of a bubble of maximum radius, R_{max} = 2.0 mm, located at an initial normalized standoff distance of 0.75 (X = 1.5 mm) from the plate, and subjected to a collapse pressure of 10 MPa. The plate is made of Al 7075 with a thickness of 5 mm. The codes were run in a two-way coupled mode. Fig. 6.21 shows the time history of the pressure and the vertical displacement at the plate center point. The interpretation of the pressure versus time profile has been previously discussed in Section 6.3.3. As the re-entrant jet impacts the plate the stresses at the surface rise above 600 MPa, largely exceeding the Al 7075 yield stress of 503 MPa used in the computation. Therefore, plastic deformation occurs within the first 0.5μs and continues to accumulate from then on.

Once the re-entrant jet impact pressures are relieved, the material deformation rate is slowed down until the second large pressures due to the toroidal bubble collapse further increase the deformation. At about

2 μs the bubble ring collapse loading vanishes and the surface starts returning as much as possible towards the initial state. However, since there was significant deviation from the elastic behavior during the loading, a permanent deformation results and the center point in the plate remains depressed by about 10 μm. One can also note successive oscillations at this center point as the stress/strain waves propagate and reflect back and forth at the rigidly held bottom and at the plate-water interface. The above dynamics illustrates the importance of the thickness of a plastic layer on the resulting deformations. No element failure or erosion was observed during this computation as the highest strain observed were 0.025, well below the failure strain limit of 0.11 for Al 7075.

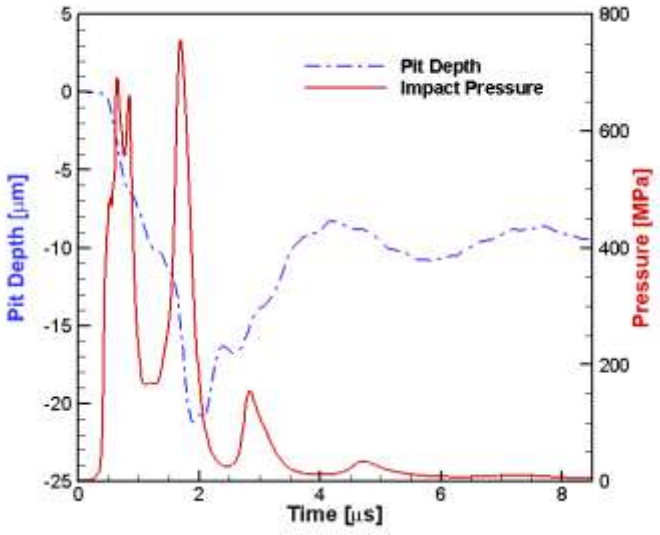

Fig. 6.21. Time history of pressure acting on an Al 7075 plate with 5 mm thickness and resulting pit depth for a collapse driving pressure of 100 atm. Initial maximum bubble radius, R_{max} = 2.0 mm. Initial bubble pressure, 1atm. Initial standoff distance from bubble center, X = 1.5 mm.

The radial extent of the permanent deformation thus computed is shown in Fig. 6.22. The figure shows the FSI simulation results for three collapse driving pressures: 6, 10 and 15 MPa. In all cases the bubble maximum radius prior to collapse was 2 mm and its standoff from the wall was 1.5 mm. The profiles of the permanent deformation generated on the plate resemble the observed pit shapes experimentally (see Fig 5.13). This profile reflects the re-entrant jet impact location at r = 0, and the location of the bubble ring, which is indicated as the secondary dip at $r \sim 0.5\ R_{max}$ in the Gaussian-like curve. Both the depth and the radius of the pit vary with the driving pressure, i.e. higher collapse pressures result in deeper and wider pits. However, it appears that the pit depth has a much stronger dependence on the collapse driving pressure, while significant permanent deformation appears to mostly occur within a radius not much larger than the maximum bubble radius, R_{max}. For the three different collapse driving pressures, the ratio of depth over radius is on the order of 10^{-2}, indicating very shallow indentations.

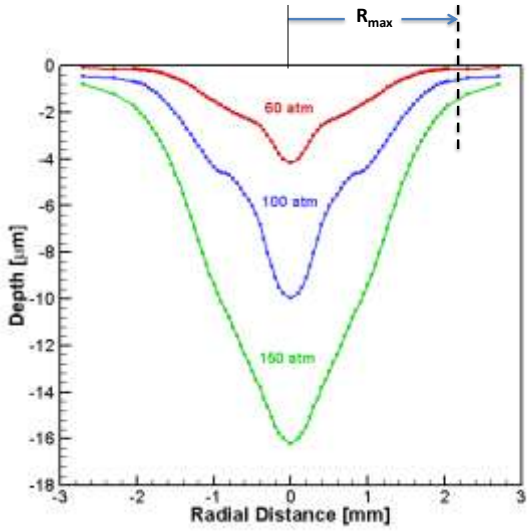

Fig. 6.22. Profile of the permanent deformation (pit depth versus r) on a 5 mm thick Al 7075 plate for different collapse driving pressures. Initial maximum bubble radius, R_{max} = 2.0 mm, and initial standoff distance, X = 1.5 mm.

6.4.3 Scaling of pit size with bubble size and driving pressure

This section examines how pit depth and pit radius vary with the maximum radius of the collapsing bubble and with the amplitude of the collapse driving pressure. Under the same conditions as in Section 6.4.2, a bubble with the maximum radius of 2 mm is made to collapse near an Al 7075 plate with a thickness of 5 mm at a standoff distance of 1.5 mm. The bubble is subjected to several collapse driving pressures, $P_{collapse}$, varying from 2 MPa to 15 MPa. As shown in Fig. 6.23 the pit depth appears to vary linearly with $P_{collapse}$ in this range. No permanent deformation occurs if $P_{impulse}$ lies below the value of the yield stress input, 503 MPa, for the Al 7075 in the model, while the permanent depth of the pit attains 24 μm at $P_{impulse}$ = 1.9 GPa.

Fig. 6.24 shows the pit radius (defined by using a cutoff depth of 1 μm) and the pit depth normalized by the maximum bubble radius. In all these FSI numerical simulations the collapse driving pressure was maintained at 10 MPa. The figure illustrates that the pit radius strongly correlates with the maximum bubble radius. The pit radius remains close to R_{max} in the full range of bubble sizes considered. This is probably a result of the fact that, at a normalized standoff of 0.75, the bubble ring formed following the re-entrant jet impact has a radius close to R_{max} and is responsible for the width (radius) of the pit.

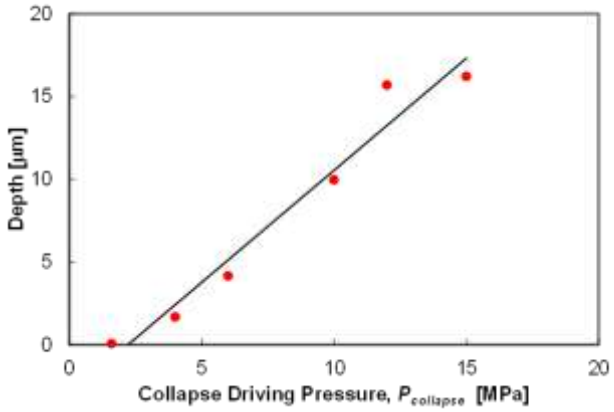

Fig. 6.23. Permanent deformation (maximum depth at the center of a 5 mm thick Al 7075 plate) for different collapse driving pressures. Initial maximum bubble radius, R_{max} = 2.0 mm. Initial standoff distance, X = 1.5 mm.

The pit depth on the other hand, appears to be more strongly dependent on R_{max} and increases as R_{max} increases. For R_{max} < 500 μm the pit depth is below the computational resolution for a collapse driving pressure of 10 MPa and a normalized standoff of 0.75.

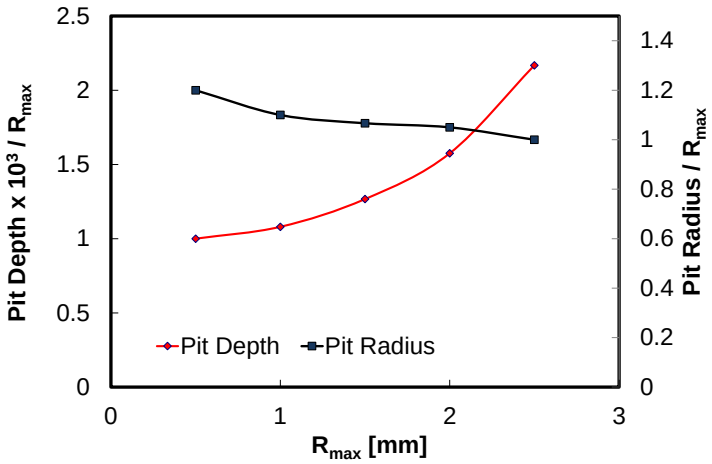

Fig. 6.24. Pit radius and pit depth for different initial maximum bubble radius, R_{max}, for bubble collapse on a 5 mm thick Al 7075 plate with the same collapse driving pressure of 10 MPa. Normalized initial standoff distance for all cases is 0.75.

Another interesting information for scaling and/or modeling is the relationship between the pit characteristics and the re-entrant jet velocity at touchdown. Fig. 6.25 shows that for jet velocities below 300 m/s there is no permanent deformation. For velocities higher than 300 m/s the pit depth and radius increase almost linearly with the re-entrant jet velocity. As previously discussed, higher jet velocities are associated with higher impact pressures (as was shown in Fig. 6.10) and this results in larger but still very low pit shape ratio (depth/radius) of less than 1 % as shown in Fig. 6.26.

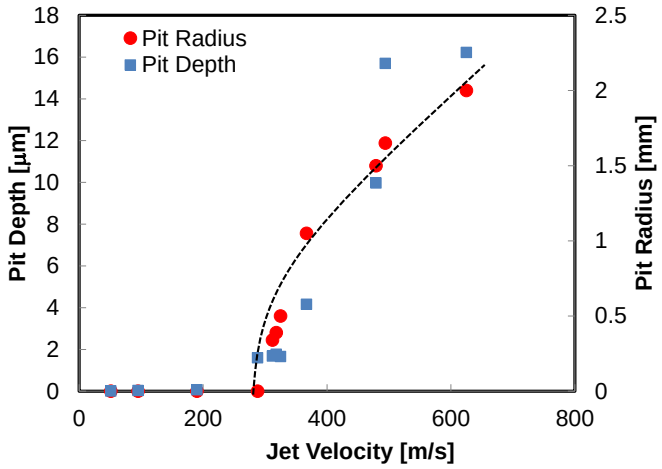

Fig. 6.25. Relationship between pit depth, pit radius, and the jet velocity. Permanent material deformation for different collapse driving pressures on a 5 mm thick Al 7075 plate. Initial maximum bubble radius, R_{max} = 2.0 mm. Initial standoff distance, X = 1.5 mm.

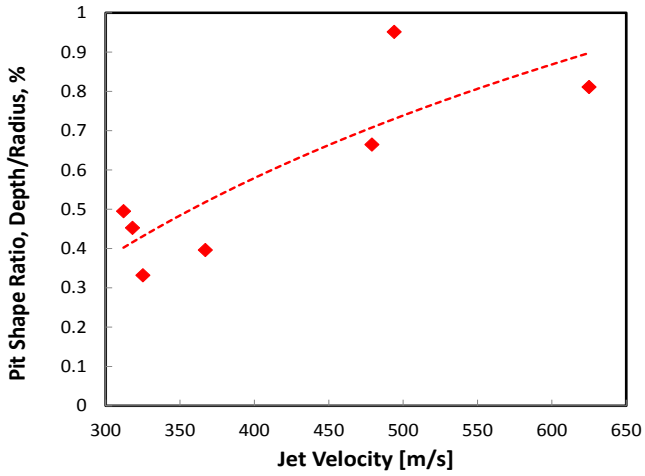

Fig. 6.26. Relationship between the pit shape ratio and the jet velocity. Permanent material deformation of a 5 mm thick Al 7075 plate for different collapse driving pressures. Initial maximum bubble radius, R_{max} = 2.0 mm. Initial standoff distance, X = 1.5 mm.

6.4.4 Effects of load duration and lateral extent on permanent deformation

The rate of application of the impulsive loads onto the material being eroded has been briefly discussed in Chapter 4, and a nano-indentation experimental technique using quasi-static application of the load to the material was proposed to deduce the impulsive loads in an inverse approach in Chapter 3. From the material response viewpoint the question should be raised as to whether the material would deform in the same way when the load is applied at a rate below or above some material characteristic response time to be sought.

In order to further understand how the impulsive pressure magnitude, duration, and radial extent relate to the material deformation, a simplified synthetic pressure loading was specified without involving the flow

field computation. The pressure loading can be described as a function of space and time with the doubly Gaussian profile:

$$P(r,t) = P_0 \, e^{-\left(\frac{t}{\Delta t}\right)^2} e^{-\left(\frac{r}{\Delta r}\right)^2} \qquad (6.15)$$

where P_0 is the maximum pressure magnitude, Δt a characteristic duration, and Δr a characteristic radial extent of the pressure loading. Except for the presence of a double peak pressure when bubbles collapse with a small standoff distance, these idealized profiles are reasonable approximations of those computed in the previous sections of this chapter and of experimental pressure loads recordings.

To extract the importance of P_0, Δt, and Δr, different pressure loads were applied on the Al 7075 plate and the deformations were computed using DYNA3D alone without FSI. Fig. 6.27 shows the pit depth and pit radius for different imposed values of P_0 when Δt and Δr are maintained constant: Δt = 0.1 μs and Δr = 250 μm.

As predicted earlier with the FSI computations (Fig. 6.23), the pit depth increases linearly with increasing load amplitude. The pit radius is also predicted to increase as the collapse pressure increases but the rate of increase drops beyond an upper limit of the load, probably because the selected Δr is kept the same.

Fig. 6.28 shows the effects of the load duration, Δt, on the pit depth and width when P_0 and Δr are kept constant (P_0 = 1 GPa and Δr = 100 μm). The figure clearly shows that both pit depth and pit radius increase nonlinearly with the duration of the applied load, Δt, up to about Δt = 2 μs in this case. For the considered values of P_0 and Δr, for Al 7075, and Δt > 2 μs, the permanent deformation becomes independent of the duration of application of the load. This implies that the dynamic effects are reduced with increasing Δt and the results become equivalent to quasi-static loading when the loading duration exceeds a certain period of time.

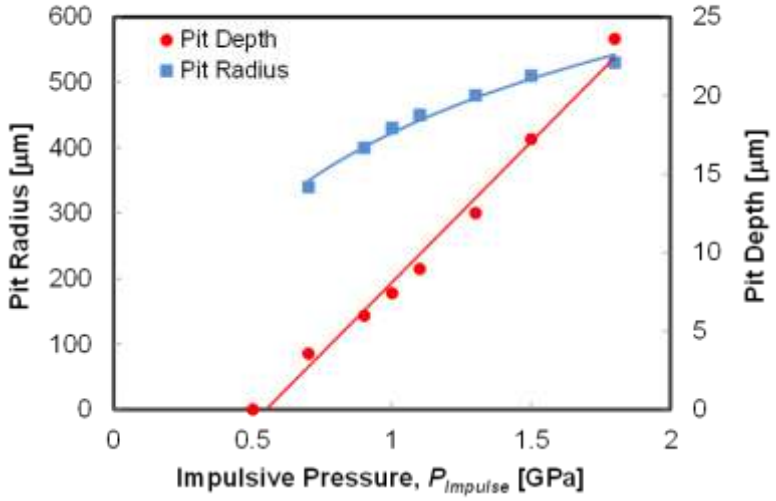

Fig. 6.27. Depth and width of the pit generated by the collapse of a bubble under a synthetic load of the form in Eq. (6.15) for different maximum pressure magnitude, P_0. The duration and radial extent were maintained constant: Δt = 0.1 μs and Δr = 250 μm. 5 mm thick Al 7075 plate.

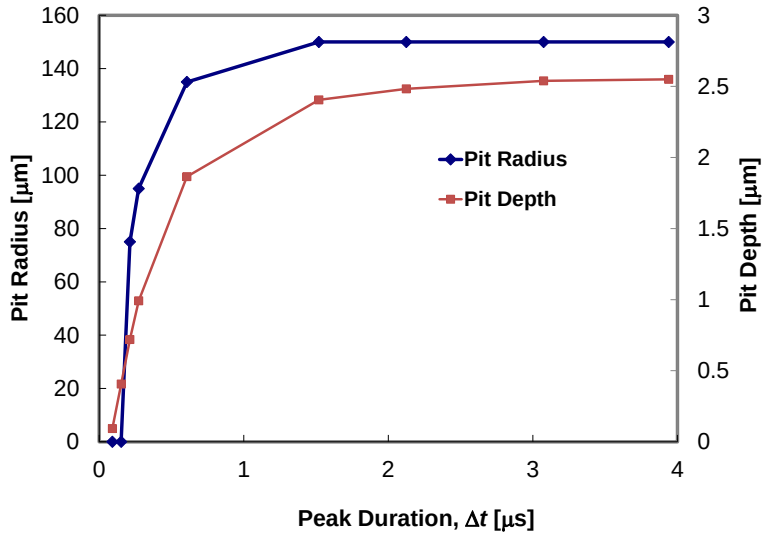

Fig. 6.28. Depth and width of the pit generated by the collapse of a bubble under a synthetic load of the form in Eq. (6.15) for different pressure durations, Δt. The pressure amplitude and lateral extent were maintained constant: P_0 =1 GPa and Δr =100 μm. 5 mm thick Al 7075 plate.

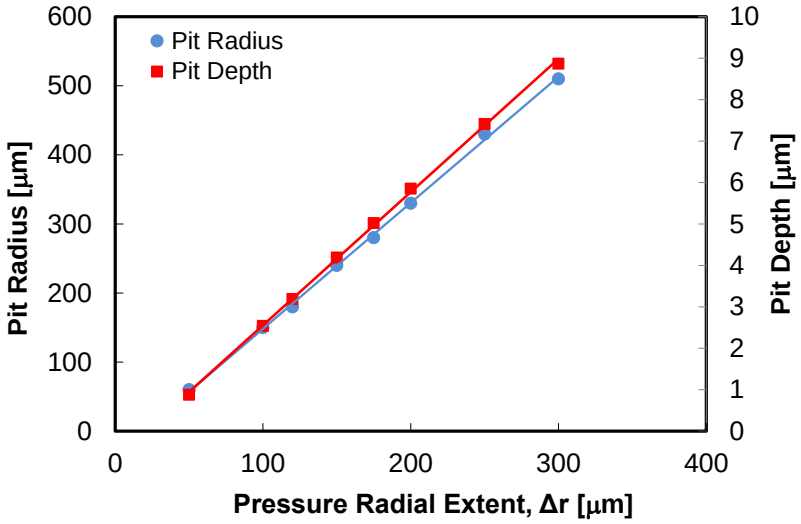

Fig. 6.29. Depth and width of the pit generated by the collapse of a bubble under a synthetic load of the form in Eq. (6.15) for different pressure lateral extent, Δr. The pressure amplitude and duration were maintained constant: P_0 =1 GPa and Δt = 0.1μs. Computations on a 5 mm thick Al 7075 plate.

Fig. 6.29 shows the effects of the radial extent of the applied load, Δr, on the pit depth and width when P_0 and Δt are kept constant (P_0 = 1 GPa, Δt = 0.1 μs). Here no saturation effect is shown (as for the peak duration shown in Fig. 6.28) and both pit depth and pit radius vary linearly with Δr. The linear variation of the pit width with Δr reconciles with what we observed in Fig. 6.24, i.e. the pit radius depends mainly on where the pressure load is imposed. The linear relationship between pit depth and Δr implies that the pit depth does not solely depend on the magnitude of the maximum pressure loading; it is also scaled with the radial extent through radial integration of the applied pressure.

6.4.5 Recovering impulsive load from material permanent deformation

This section addresses the potential of using pitting tests as a means of characterizing the cavitation flow field intensity. We consider as an illustration a series of computations, where a bubble of initial maximum radius 400 □m at equilibrium in a liquid of ambient pressure 0.1 MPa is subjected to a pressure rise to various maximum pressure levels, $P_{collapse}$, leading to energetic collapse. The bubble center is initially 400 □m away from a plate made of a material with known properties. Two-way fluid-structure interaction computations following the procedures described in the previous sections were conducted using GEMINI and DYNA3D. The computational results include bubble dynamics, pressure loads at the liquid-wall interface, and resulting material stresses, strains, and deformations. Four different values of $P_{collapse}$: 5, 6, 7, and 10 MPa, which resulted in $P_{impulse}$: 0.8, 1.2, 2.15, and 3.4 GPa, were used for all four materials studied earlier: NAB, stainless steel A2205, and aluminum Al 7075, and Al 1100-H19.

Fig. 6.30 and Fig. 6.31 present the normal stresses σ_{nn} on the material during the bubble collapse for two values of $P_{collapse}$: 5 MPa and 10 MPa. Both figures show the influence of fluid-structure interaction on the results. When the response of the material, its deformation, and its feedback to the flow field are included, the normal stresses are noticeably reduced as compared to the rigid wall case. For $P_{collapse}$ = 5 MPa, all four materials feel practically the same normal stresses, which are about 20% lower than those felt by the rigid body (Fig. 6.30). For the higher excitation, $P_{collapse}$ = 10 MPa, normal stresses show further decrease as the material gets softer, with the peak stresses almost 50% lower than those felt by the rigid body for Al 1100-H19 (Fig. 6.31). This effect has been observed experimentally in [50] through water jet impacting on an instrumented deformable plate; the measured pressures were significantly lower than when impacting a rigid plate.

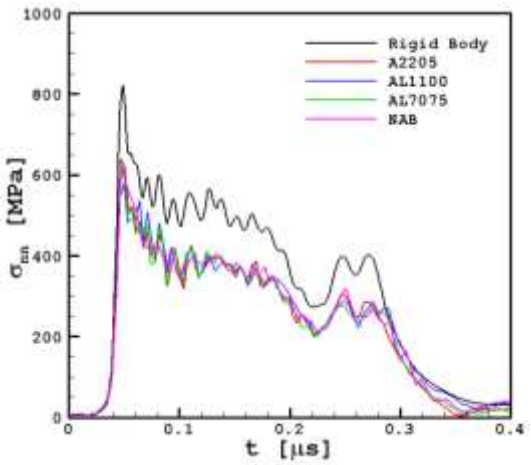

Fig. 6.30. *Normal stress component on the first plate element below the interface plate-water at the bubble axis. The stresses are the material response to an impulsive loading due to a bubble collapse over the plate. The bubble had an initial radius of 400 μm and was located above the plate at a distance of 400 μm to the bubble center. The collapsing bubble is driven by pressure rise from 0.1 MPa to 5 MPa.*

This behavior may originate from the unsteadiness in the case of a deforming target. For a rigid flat wall, there is a direct balance between the normal impact force and the integral of the normal stresses, i.e. balance between the impact pressure, p, and the normal stress:

$$\int p\mathbf{n}ds = \int \sigma_{nn}\mathbf{n}ds \qquad p = \sigma_{nn} \tag{6.16}$$

For a deforming plate, an additional momentum term exists,

$$\int p\mathbf{n}ds = \int \sigma_{nn}\mathbf{n}ds + \int \gamma dm \qquad \gamma : \text{normal acceleration} \qquad (6.17)$$

The presence of the acceleration term reduces the value of σ_{nn}.

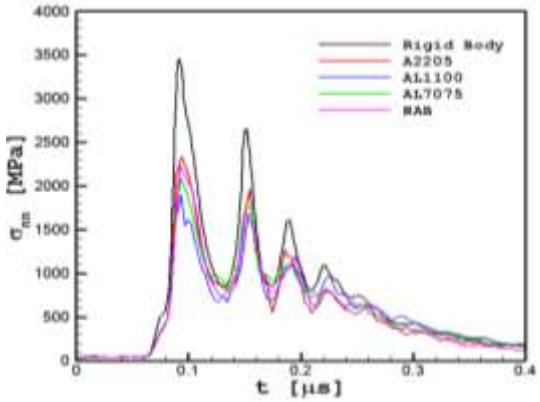

Fig. 6.31. *Normal stress component on the first plate element below the interface plate-water at the bubble axis. The bubble had an initial radius of 400 μm and was located above the plate at a distance of 400 μm to the bubble center. The collapsing bubble is driven by pressure rise from 0.1 MPa to 10 MPa.*

Another important reason for the reduction in σ_{nn} is geometric. As the boundary deforms it deflects the impacting re-entrant jet and modifies the incoming pressure waves. This results in the otherwise only normal energy on the flat plate to become split between normal and other direction stresses. Fig. 6.32 shows the radial stresses σ_{rr} on the first element below the free surface of the plate. The amplitude of σ_{rr} is of the same order of σ_{nn} explaining the noticeable reduction of the normal component. This amplitude is also seen to increase for the softer materials.

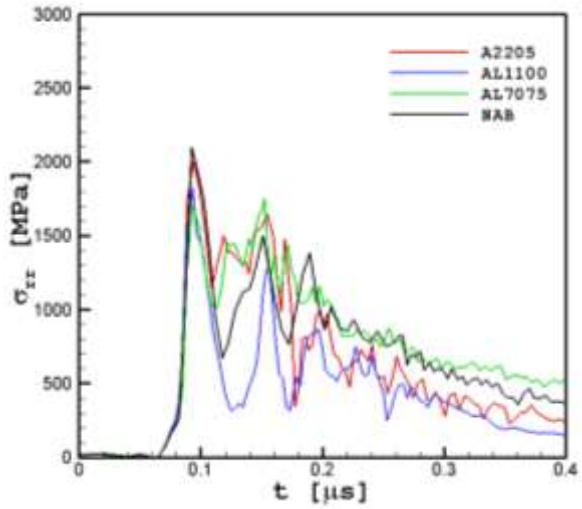

Fig. 6.32. *Radial stress component on the first element below the free surface of the plate at the bubble axis. The bubble had an initial radius of 400 μm and was located above the plate at a distance of 400 μm to the bubble center. The collapsing bubble is driven by pressure rise from 0.1MPa to 10MPa.*

For simple uniaxial loading, a material will start yielding if the stress exceeds the material yield stress. For complex loading conditions as it is the case for a cavitation impact, a three-dimensional system of stresses including normal and shear stresses develops in the material. To decide whether the combination of stresses will result in yielding, the Von Mises stress or equivalent stress may be computed and

compared to the material yield stress. Fig. 6.33 shows the equivalent stresses computes in the first element at the surface of each material for the same computations as in Fig. 6.31 and 6.32. One should note the sharp change in slope when the stresses approach the yield stress, partially explaining the stress drop. From that point on, the material follows the plastic portion of the stress-strain curve, which has a much milder slope, thus resulting in a significant change of the slopes of stress versus time and a significant reduction in the value of the maximum equivalent stress relative to the imposed impulsive pressure.

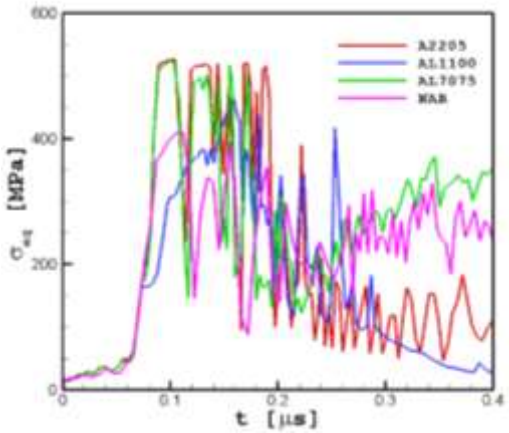

Fig. 6.33. *Equivalent stress on the first element below the free surface of the plate at the bubble axis. The bubble had an initial radius of 400 μm and was located above the plate at a distance of 400 μm to the bubble center. The collapsing bubble is driven by pressure rise from 0.1 MPa to 10 MPa.*

Fig. 6.34 shows the vertical displacement versus time for the four materials. It is this quasi-final deformation that is remaining in the pits after exposure of the materials to the impulsive loads due to the bubble collapse. The much larger maximum deformation in each of the curves of Fig. 6.34 is not recorded by the material and is unknown to the observer of the pit characteristics. The lengthy computations in Fig. 6.34 were stopped at 3 μs, a relatively very long time after the loads due to the bubble collapse have died out (see Fig. 6.31 and Fig. 6.32). However, computations for a longer duration are needed until no change in the depth is observed; nevertheless the conclusions drawn here will not change significantly but towards slightly smaller permanent deformations.

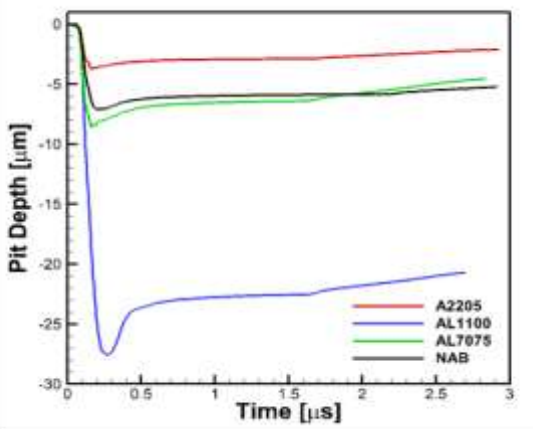

Fig. 6.34. *Normal displacement of a node located on the surface of the plate at the axis, indicating the evolution of pit depth. The bubble had an initial radius of 400 μm and was located above the plate at a distance of 400 μm to the bubble center. The collapsing bubble is driven by a pressure rise from 0.1 MPa to 10 MPa.*

An observer will measure the depth of the pit, *h*, and the pit diameter, *D*, obtained after using a cutoff depth value (e.g. 1 μm) as described in Chapter 3. An inverse computation of the load could then be made based on the method described in Section 3.4. Using the relationship between mean strain, ε_{mean}, and the pit geometric aspect ratio, h/D, where h is the surface deformation induced by an impact (see Fig. (6.35)), the mean strain can be computed as (see Eq. (3.12)):

$$\varepsilon_{mean} \cong 0.8\frac{h}{D} \tag{6.18}$$

If we use an analysis similar to that done in [51, 52], we can deduce the relationship between the maximum strain, $\varepsilon_{\max}$, and the mean strain, ε_{mean}. Fig. 6.35 shows an idealized sketch of the plastic zone of the cavitation pit, which is similar to Fig. 3.18.

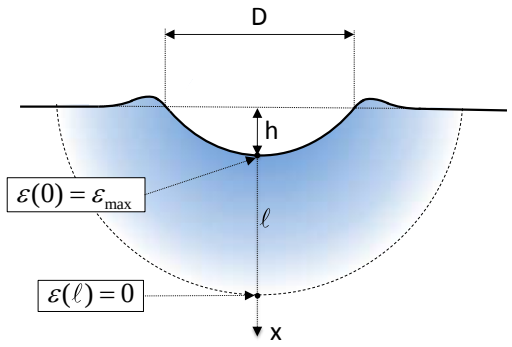

Fig. 6.35. Idealized plastic zone diagram due to spherical indentation

In Fig. 6.35, it is assumed that the maximum strain, $\varepsilon_{\max}$, occurs on the pit surface and decreases gradually to zero on the boundary of the plastic zone within a radial distance ℓ. In the plastic zone, $\varepsilon(x)$ can be expressed as:

$$\varepsilon(x)=\varepsilon_{\max}\left(1-\frac{x}{\ell}\right)^{\theta} \tag{6.19}$$

where x is the radial distance from the pit surface and θ is a material parameter that defines the sharpness of the strain gradient around the impact.
By integrating $\varepsilon(x)$ from 0 to ℓ using Eq. (6.19) and dividing by ℓ, we obtain the mean strain:

$$\varepsilon_{mean} = \frac{\varepsilon_{\max}}{\theta+1} \tag{6.20}$$

Combining Eqs. (6.18) and (6.20), we obtain:

$$\varepsilon_{\max} \cong (\theta+1)\,0.8\frac{h}{D} \tag{6.21}$$

Typically, the maximum strain is 3 to 5 times the mean strain. The actual θ values were obtained experimentally using the nanoindentation method for three different materials: Al 7075, NAB and SS A2205 (see Fig. 7.2). These values are 2.0 for Al 7075, 2.8 for NAB and 2.2 for SS A2205. In the exercise summarized in Table 6.2, we used $\varepsilon_{\max}$ values obtained from Eq. (6.21) with the experimental θ values for the three materials. We also used, for order or magnitude evaluation, the value $\theta=2.0$ for Al 1100 (the same value as for Al 7075) since an experimental value is not available.

Using the stress-strain relationship in Fig. 6.20, an effective stress (i.e. surface load) can be deduced from $\varepsilon_{\max}$. Table 6.2 shows, for the four values of the maximum impulsive pressure $P_{impulse}$ considered here: (i) the maximum normal stress at material surface, (ii) the maximum equivalent stress, both obtained by the

FSI computations, and (iii) the stress deduced from Eq. (6.21) after obtaining the material deformation and recording h and D for a cutoff depth of 1 μm.

The two smaller peak pressures generated by the bubble collapse in Table 6.2, $P_{impulse} = 0.8\,GPa$ and $1.2\,GPa$, imposed to the materials are missed by the three harder materials: NAB, SS A2205, and Al 7075 because the Von Mises stress within the material does not reach the elastic limit. They do, however, both result in a pit in Al 1100 due to its lower elastic limit. Obviously, the use of softer materials allows extending the range of impact loads to smaller values. When pits were produced, the stresses deduced from the pit analysis appear to be close under almost all conditions to the maximum equivalent stresses in the material.

Table 6.2. Impulsive pressure loads, $P_{impulse}$, imposed in the computation, resulting maximum equivalent stresses in the material and stress values deduced from the computed pits resulting from permanent deformation and Eq. (6.21). Pit diameter was computed using a cutoff depth of 1 μm. Bold values correspond to maximum equivalent stresses exceeding yield stress.

Material	Yield stress [MPa]	Stress [MPa]	Bubble Impulsive Pressure Peak $P_{impulse}$ [MPa]			
			800	1200	2150	3400
NAB	360	Max normal stress at material surface	606	879	1452	2196
		Max equivalent stress	360	**365**	**396**	**455**
		Stress deduced from pit	no pit	no pit	508	585
SS A2205	515	Max normal stress at material surface	628	888	1506	2310
		Max equivalent stress	511	515	**520**	**536**
		Stress deduced from pit	no pit	no pit	no pit	605
Al 7075	503	Max normal stress at material surface	608	900	**1407**	**2082**
		Max equivalent stress	503	503	**510**	**558**
		Stress deduced from pit	no pit	no pit	590	630
Al 1100	165	Max normal stress at material surface	570	829	1247	1878
		Max equivalent stress	**214**	**263**	**390**	**574**
		Stress deduced from pit	280	410	510	555

6.5 Summary

This chapter addressed the mechanisms of impulsive load generation on a rigid or deforming solid boundary from the collapse of a single bubble. The effects of the bubble maximum equivalent radius, R_{max}, the collapse driving pressure (i.e. the local pressure driving the bubble collapse), the bubble standoff from the boundary, and the plate material properties were investigated.

By means of a hybrid incompressible-compressible method, the computed pressures on the wall showed two major components: a water hammer pressure from the impact of the re-entrant jet on the solid surface and a shock wave pressure emitted from the bubble at or near its minimum volume (see Fig. 6.6). The re-entrant jet impact pressure is proportional to the product of the liquid impedance (product of sound speed and density of the liquid, ρc) and the re-entrant jet impact speed on the solid surface, V_{jet}. It has in general a lower value than the ideal water hammer pressure resulting from a water column impacting normally on a flat solid surface. It approaches this ideal value, $\rho c V_{jet}$, for very high collapse driving pressures. The shock waves can be spherical for bubbles at large standoff from the wall or toroidal for bubbles collapsing very close to the wall. In the region of normalized standoff, $X/R_{max}<1$, both pressure types (water hammer and shock wave) appear to generally have the same order of magnitude.

The cavitation impulsive pressures strongly depend on the cavitation collapse driving pressure and to a much lesser extent on the bubble maximum radius, R_{max}. Indeed, both the re-entrant jet velocity and the bubble equivalent radius velocity depend on the square root of the cavitation collapse driving pressure and are independent of R_{max}. However, the loads imparted to the material depend on thearea of the impacted or influenced region of the material and depend thus on R_{max}^2. As a result the actual pit diameter depends on R_{max}.

Study of two-way fluid-structure interaction for a bubble collapsing near a plastically deforming material shows the importance of not only the impulsive pressure amplitude but also its duration and radial extent. These finite quantities (duration and radial extent) directly affect the dimensions of the permanently deformed regions of the surface (pits). The unsteady response dependency on the impulsive load duration implies the existence of a material characteristic response time, which should be investigated in future studies.

The idea of deducing cavitation impact loads from basic nano-indentation equations applied to measured or computed pits was investigated. The analysis provided in this chapter shows that such an approach provides a good idea of the generated equivalent stresses in the material. However, in order to obtain the liquid generated pressures and enable accurate quantitative cavitation pressure field characterization, additional considerations and improvements are needed.

References

1. Chahine GL, Perdue TO, Tucker CB (1988) Interaction between an underwater explosion bubble and a solid submerged structure. DYNAFLOW, INC., Technical Report 89001-1, September 1988
2. Chahine GL, Perdue TO (1988) Simulation of the three-dimensional behavior of an unsteady large bubble near a structure. Drops and Bubbles, Third International Colloquium, Monterey, CA, ed. Taylor G. Wang, pp.188-199
3. Chahine GL, Kalumuck KM (1998) BEM software for free surface flow simulation including fluid-structure interaction effects. International Journal of Computer Applications in Technology 11(3/4/5):177-198
4. Kalumuck KM, Duraiswami R, Chahine GL (1995) Bubble dynamics fluid-structure interaction simulation by coupling fluid BEM and structural FEM codes. Journal of Fluids and Structures 9:861-883
5. Kalumuck KM, Duraiswami R, Chahine GL (1995) Analysis of the response of a deformable structure to underwater explosion bubble loading using a fully coupled fluid-structure interaction procedure. SAVIAC Proceedings of the 66th Shock and Vibration Symposium, Volume I, Biloxi, MS
6. Chahine GL, Duraiswami R (1993) Method for calculating 2-D and 3-D underwater explosion bubble behavior in free water and near structures. NSWC Dahlgren Division Report NSWCDD/TR-93/44
7. Chahine GL, Duraiswami R, Kalumuck KM (1996) Boundary element method for calculating 2-d and 3-d underwater explosion bubble loading on nearby structures including fluid-structure interaction effects. NSWC Dahlgren Div. Rpt. NSWCDD/TR-93/46
8. Wardlaw AB, Luton JA, Renzi JR, Kiddy KC, McKeown RM (2003) The GEMINI Euler solver for the coupled simulation of underwater explosions. NSWCIHD/IHTR-2500
9. Wardlaw A Jr, Luton JA (2000) Fluid-structure interaction for close-in explosions. Shock and Vibration Journal 7:265-275
10. Wardlaw A Jr, Luton JA, Renzi JJ, Kiddy K (2003) Fluid-structure coupling methodology for undersea weapons. Fluid Structure Interaction II, WIT Press, pp. 251–263
11. Chahine GL, Raju R, Hsiao C-T (2010) Simulation of the impact pressures from non-spherical bubble collapse near a wall: Handback from 3DYNAFS© to GEMINI. DYNAFLOW, INC. Tech. Report, 2M2M9007-NSWCIH-1
12. Hsiao C-T, Chahine GL (2010) Incompressible-compressible link to accurately predict wall pressure. SAVIAC, 81st Shock and Vibration Symposium, Orlando, FL, October 24-28, 2010
13. Whirley RG, Engelmann BE (1993) DYNA3D: A nonlinear, explicit, three dimensional finite element code for solid and structural mechanics - user manual, Lawrence Livermore National Laboratory, UCRL-MA-107254, Rev. 1
14. Chahine GL, Hsiao C-T (2012) Modeling microbubble dynamics in biomedical applications. Journal of Hydrodynamics 24 (2):169-183
15. Hsiao C-T, Chahine GL, Liu H-L (2003) Scaling effects on prediction of cavitation inception in a line vortex flow. Journal of Fluids Engineering 125:53-60
16. Jameson A, Schmidt W, Turkel E (1981) Numerical simulation of the Euler equations by finite volume methods using Runge-Kutta time stepping schemes. AIAA paper 81-1259
17. Luton JA, Wardlaw A, Chahine GL, Hsiao C-T (2004) Simulation of surface vessel hull whipping response using fully-coupled hydrocodes. SAVIAC, 75th Shock and Vibration Symposium, October 18-22, 2004

18. Wardlaw AB, Luton JA, Renzi JR, Kiddy KC, McKeown RM (2003) The GEMINI Euler solver for the coupled simulation of underwater explosions. NSWCIHD/IHTR-2500
19. Plesset MS, Chapman RB (1971) Collapse of an initially spherical vapour cavity in the neighborhood of a solid boundary. Journal of Fluid Mechanics 47 (2):283-290
20. Ellis AT (1965) Parameters affecting cavitation and some new methods for their study. California Institute of Technology, Rep E-115.1
21. Naude CF, Ellis AT (1961) On the mechanism of cavitation damage by non-hemispherical cavities collapsing in contact with a solid boundary. Trans. ASME, Journal of Basic Engineering 83 (4):648-656
22. Blake JR, Taib BB, Doherty G (1986) Transient cavities near boundaries. Part I. Rigid boundary. Journal of Fluid Mechanics 170 (September):479-497
23. Zhang S, Duncan H, Chahine GL (1993) The final stage of the collapse of a cavitation bubble near a rigid wall. Journal of Fluid Mechanics 257 (December):147-181
24. Jayaprakash A, Chahine GL, Hsiao C-T (2012) Numerical and experimental study of the interaction of a spark-generated bubble and a vertical wall. Journal of Fluids Engineering 134:031301. doi:10.1115/1.4005688
25. Chahine GL, Annassami R, Hsiao C-T, Harris GS (2006) Scaling rules for the prediction of UNDEX bubble re-entering jet parameters. Critical Technologies in Shock and Vibration, Ed. Walter Pilkey, 4(1):1-12
26. Harris GS, Ilamni RZ, Lewis W, Rye K, Chahine GL (2009) Underwater explosion bubble phenomena tests near a simulated dam structure. Naval Surface Warfare Center, Indian Head Division IHTR 10-3055, November 2009
27. O'Daniel JL, Harris G, Ilamni R, Chahine GL, Fortune J (2011) Underwater explosion bubble jetting effects on infrastructure. US Army Engineer Research and Development Center Report, DTIC, PDF Url: ADA545705, 31 March 2011
28. Harris G (2010) Multiple UNDEX bubble interaction tests. SAVIAC, 81st Shock and Vibration Symposium, Orlando, FL, October 24 – 28
29. Lin JI (2005) DYNA3D: A nonlinear, explicit, three-dimensional finite element code for solid and structural mechanics. User Manual, Laurence Livermore National Laboratory, UCRL-MA-107254, January
30. van Wijngaarden L (1964) On the collective collapse of a large number of gas bubbles in water. Proc. 11th Int. Conf. Appl. Mech., Springer-Verlag, Berlin, 854-861
31. Mørch KA (1979) Dynamics of cavitation bubbles and cavitating liquids. Treatise on Materials Science and Technology 16:309-355
32. d'Agostino L, Brennen CE (1983) On the acoustical dynamics of bubble clouds. ASME Cavitation and Polyphase Flow Forum, Houston, 72-76
33. Chahine GL (1983) Cavitation cloud theory. Proceedings, 14th Symposium on Naval Hydrodynamics, Ann Arbor, Michigan, National Academy Press, pp. 165-194, Washington, D.C.
34. Bremond N, Arora M, Ohl C-D, Lohse D (2006) Controlled multibubble surface cavitation. Physical Review Letters A 96 (22):224501
35. Chahine GL, Liu HL (1985) A singular perturbation theory of the growth of a bubble cluster in a superheated liquid. Journal of Fluid Mechanics 156 (July):257-279
36. Chahine GL, Duraiswami R (1992) Dynamical interaction in a multi-bubble cloud. Journal of Fluids Engineering 114 (4):680-686
37. Chahine GL (2005) Numerical studies of the interaction of multiple underwater explosion bubbles. Critical Technologies in Shock and Vibrations. Ed. Walter Pilkey 3 (1):1-13
38. Harris G (2010) Small scale UNDEX bubble-dam interaction tests. SAVIAC, 81st Shock and Vibration Symposium, Orlando, FL, October 24-28, 2010
39. Chahine GL (1991) Dynamics of the interaction of non-spherical cavities. Mathematical Approaches in Hydrodynamics, ed. T. Miloh, SIAM Publications
40. Chahine GL, Hsiao C-T, Raju R (2013) Scaling of cavitation bubble cloud dynamics on propellers. In Kim KH, Chahine GL, Franc J-P, Karimi A (eds.) Advanced Experimental and Numerical Techniques for Cavitation Erosion Prediction, Series Fluid Mechanics and Its Applications, Springer
41. Knapp RT, Daily JW, Hammitt FG (1970) Cavitation. McGraw Hill Book Co., NY
42. Hammitt FG (1980) Cavitation and Multiphase Flow Phenomena. McGraw-Hill International Book Co., NY
43. Young FR (1989) Cavitation. McGraw Hill Book Co., NY
44. Blake JR, Gibson DC (1987) Cavitation bubbles near boundaries. Annual Review of Fluid Mechanics 19:99-123
45. Best JP (1993) The formation of toroidal bubbles upon the collapse of transient cavities. Journal of Fluid Mechanics 251 (June):79-107
46. Brujan EA, Keen GS, Vogel A, Blake JR (2002) The final stage of the collapse of a cavitation bubble close to a rigid boundary. Physics of Fluids 14 (1):85-92
47. Krieger J, Chahine GL (2005) Acoustic signals of underwater explosions near surfaces. Journal of Acoustical Society of America 118 (5):2961-2974
48. Chahine GL (1982) Experimental and asymptotic study of nonspherical bubble collapse. Applied Scientific Research 38:187-197
49. www.matweb.com (material property data)
50. Chahine GL, Kalumuck KM (1998) The Influence of Structural Deformation on Water Jet Impact Loading. Journal of Fluids and Structures 12 (1):103-121, January
51. Karimi A, Leo WR (1987) Phenomenological model for cavitation erosion rate computation. Materials Science Engineering 95:1-14
52. Francis HA (1976) Phenomenological Analysis of Plastic Spherical Indentation. J. of Engineering Materials and Technology 98 (3):272-281